

# 1 **Advanced Manufacturing for Electrosynthesis of Fuels** 2 **and Chemicals from CO<sub>2</sub> – Supplemental Information**

3 Daniel Corral<sup>1,2,†</sup>, Jeremy T. Feaster<sup>3,†</sup>, Sadaf Sobhani<sup>4</sup>, Joshua R. DeOtte<sup>1</sup>, Dong Un Lee<sup>2</sup>,  
4 Andrew A. Wong<sup>1</sup>, Julie Hamilton<sup>1</sup>, Victor A. Beck<sup>4</sup>, Amitava Sarkar<sup>2,3,5</sup>, Christopher Hahn<sup>6,\*</sup>,  
5 Thomas F. Jaramillo<sup>2,6,\*</sup>, Sarah E. Baker<sup>3,\*</sup>, and Eric B. Duoss<sup>1,\*</sup>

6 <sup>1</sup> Materials Engineering Division, Lawrence Livermore National Laboratory, Livermore,  
7 CA 94550, United States

8 <sup>2</sup> SUNCAT Center for Interface Science and Catalysis, Department of Chemical  
9 Engineering, Stanford University, Stanford, CA 94305, USA

10 <sup>3</sup> Materials Science Division, Lawrence Livermore National Laboratory, Livermore, CA  
11 94550, United States

12 <sup>4</sup> Computational Engineering Division, Lawrence Livermore National Laboratory,  
13 Livermore, CA 94550, United States

14 <sup>5</sup> Total EP Research & Technology USA, LLC., Houston, TX 77002, USA

15 <sup>6</sup> SUNCAT Center for Interface Science and Catalysis, SLAC National Accelerator  
16 Laboratory, Menlo Park, CA 94025, USA

17 † These authors contributed equally to this work.

18 \*Correspondence: [chahn@slac.stanford.edu](mailto:chahn@slac.stanford.edu), [jaramillo@stanford.edu](mailto:jaramillo@stanford.edu), [baker74@llnl.gov](mailto:baker74@llnl.gov),  
19 and [duoss1@llnl.gov](mailto:duoss1@llnl.gov) □

## 20 **Table of Contents**

21	<b><i>Experimental Methods</i></b> _____	<b>6</b>
22	<b>Reactor Manufacturing</b> _____	<b>6</b>
23	<b>System Design</b> _____	<b>7</b>
24	<b>Electrolyte and Electrode Preparation and Characterization</b> _____	<b>8</b>
25	<b>Electrochemical Experiments with Temperature Measurement</b> _____	<b>9</b>
26	<b>Calculations for Cathodic Energy Efficiency</b> _____	<b>10</b>
27	<b>Modeling of AM Electrochemical System</b> _____	<b>11</b>
28	<b>Calculations for Product Yield</b> _____	<b>14</b>
29	<b><i>Supplemental Figures</i></b> _____	<b>15</b>
30	<b>Figure S1. Photograph of advanced manufactured reactor system during setup and pre-</b>	
31	<b>electrolysis.</b> _____	<b>15</b>
32	<b>Figure S2. Simplified system design for electrochemical CO<sub>2</sub> reduction experiments.</b> _____	<b>16</b>
33	<b>Figure S3. Detailed drawing of Generation 3 Reactor.</b> _____	<b>17</b>
34	<b>Figure S4. Schematic representation of the species transport in the Generation 3 reactor.</b>	<b>18</b>
35	<b>Figure S5. Schematic representation of the computational domain.</b> _____	<b>19</b>
36	<b>Figure S6. SEM micrographs of Cu-catalyst coated expanded-PTFE.</b> _____	<b>20</b>
37	<b>Figure S7. X-ray photoemission spectroscopy (XPS).</b> _____	<b>21</b>
38	<b>Figure S8. X-ray diffraction (XRD).</b> _____	<b>22</b>
39	<b>Figure S9. PEIS for generations of reactors.</b> _____	<b>23</b>

40	Figure S10. ECSA measurement of surface area. _____	24
41	Figure S11. Partial current densities (PCDs) of 2-carbon products for various inlet CO <sub>2</sub> flow	
42	rates. _____	25
43	Figure S12. Average number of electrons transferred to CO <sub>2</sub> -reduced products. _____	26
44	Figure S13. Faradaic efficiencies and potential vs RHE as a function of geometric current	
45	density for 10 sccm. _____	27
46	Figure S14. Partial current densities for hydrogen, single-carbon products, and CO <sub>2</sub> R as a	
47	function of potential vs RHE at 10 sccm. _____	28
48	Figure S15. Cathodic energy efficiency as function of potential vs RHE at 10 sccm. _____	29
49	Figure S16. Stability of performance of AM-VFR. _____	30
50	Figure S17. Contact angle measurements. _____	31
51	Figure S18. COMSOL model showing location of temperature probes during electrolysis. _	32
52	Figure S19. Ethanol concentration profiles for 10 sccm _____	33
53	Figure S20. Concentration profiles for species participating in homogenous reaction within	
54	aqueous electrolyte for various current densities. (a) _____	34
55	Figure S21. pH profiles within aqueous electrolyte for various current densities. (a). _____	35
56	Figure S22. CO <sub>2</sub> concentration profile for a subset of the domain around the catalyst layer.	
57	_____	36
58	Figure S23. CO <sub>2</sub> concentration as a function of liquid penetration depth into the diffusion	
59	media for various current densities. _____	37

60	Figure S24. Simulation results for CO <sub>2</sub> concentration at the CL at 10 sccm as a function of	
61	penetration depth into the DM. _____	38
62	Figure S25. CO <sub>2</sub> depletion at the inlet of the catalyst layer as a function of current density.	
63	_____	39
64	Figure S26. Measured fraction of CO <sub>2</sub> R current towards C <sub>2+</sub> products. _____	40
65	Figure S27. Measured ratio of CO <sub>2</sub> R to HER. _____	41
66	Figure S28. Gas evolution of products over the course of the experiment. _____	42
67	Figure S29. Comparison of results performed at different sites. _____	43
68	Figure S30. Comparison of literature for yield plots. _____	44
69	Figure S31. X-ray Computed Tomography (XCT) of GDE. _____	45
70	<b><i>Supplemental Tables</i></b> _____	<b>46</b>
71	Table S1. Forward and backward reaction coefficient values for Equations 1 and 2. _____	46
72	Table S2. Average values at 5 sccm CO <sub>2</sub> flow rate. _____	47
73	Table S3. Standard deviation values at 5 sccm CO <sub>2</sub> flow rate. _____	47
74	Table S4. Average values at 10 sccm CO <sub>2</sub> flow rate. _____	48
75	Table S5. Standard deviation values at 10 sccm CO <sub>2</sub> flow rate. _____	48
76	Table S6. Average values at 20 sccm CO <sub>2</sub> flow rate. _____	49
77	Table S7. Standard deviation values at 20 sccm CO <sub>2</sub> flow rate. _____	49
78	Table S8. Average values at 40 sccm CO <sub>2</sub> flow rate. _____	50
79	Table S9. Standard deviation values at 40 sccm CO <sub>2</sub> flow rate. _____	50

80	<b>Table S10. Average values for reactor generation 1-3.</b> _____	<b>51</b>
81	<b>Table S11. Standard deviation values for reactor generations 1-3.</b> _____	<b>51</b>
82	<b>Table S12. Yield Comparison with literature.</b> _____	<b>52</b>
83	<b><i>References</i></b> _____	<b>53</b>
84		
85		

## 86 **Experimental Methods**

### 87 **Reactor Manufacturing**

88           Manufacturing costs and time to create reactor components for conventional manufacturing  
89 were based on estimates provided by Lawrence Livermore National Laboratory and Stanford  
90 University machine shops; costs and times for advanced manufacturing were based on printer  
91 calculations. While many reactors were produced, they can be generally classified as one of three  
92 generations of reactor design. The first generation was inspired by previous work in the field<sup>1,2</sup>  
93 and consists of three compartments: (1) cathode gas compartment, (2) catholyte compartment, and  
94 (3) anolyte compartment. Each of the compartments were 15 mm thick. The second generation of  
95 reactors used a similar design as the first and also contained three compartments; the major change  
96 employed was to reduce the thickness of each of the compartments to 7 mm, which reduced the  
97 distance between the cathode and anode from 30 mm to 14 mm. Both Generation 1 and 2 reactors  
98 used the system schematic shown in Figure S2a. The third generation of reactors maintained the 7  
99 mm thick compartments and introduced a fourth, anolyte gas compartment to aid with gas  
100 management on the anode. Generation 3 reactors used the system schematic shown in Figure S1b  
101 for electrochemical experiments.

## 102 **System Design**

103           The reactor schematics used for all experiments is shown in Figure S2. The 3D printed  
104 reactors were assembled and sealed using silicone gaskets. The catholyte and anolyte sparging  
105 chambers contained 15 mL each of prepared 1 M KHCO<sub>3</sub> electrolyte (see electrolyte preparation  
106 in the following section). The electrolytes were circulated from the chambers to their respective  
107 compartments in the VFR using peristaltic pumps (Cole-Palmer) at 5 mL min<sup>-1</sup> to minimize local  
108 accumulation of product. Research-grade CO<sub>2</sub> (Praxair, 5.0) was flown into the cathode gas  
109 compartment of the reactors of Generations 1 and 2, as well as the cathode and anode gas  
110 compartments of Generation 3 reactors; in the latter configuration, the reactant gas carried gas  
111 products from the reactor back to the sparging chambers. Gas products formed at the cathode were  
112 delivered to an in-line gas chromatograph (SRI Instruments) for regular measurements at 15-  
113 minute increments; oxygen formed on the anode was sent to the exhaust. At the conclusion of each  
114 experiment, the electrolyte for each chamber was collected. Liquid products formed on the cathode  
115 were analyzed by <sup>1</sup>H NMR (500 MHz, Avance III HD Bruker with Prodigy cryoprobe) calibrated  
116 with a water and salt suppression standard.

## 117 **Electrolyte and Electrode Preparation and Characterization**

118           The electrolyte was made by bubbling CO<sub>2</sub> into 0.5 M K<sub>2</sub>CO<sub>3</sub> solution (Alfa-Aesar,  
119 99.998%) for 30 minutes to convert the solution to 1 M KHCO<sub>3</sub>. Chelex® beads (Sigma-Aldrich)  
120 were then added at a ratio of 10 g for every L solution to remove any trace metal impurities from  
121 the electrolyte. The Chelex® beads are filtered out of the electrolyte prior to injection into the  
122 catholyte and anolyte chambers.

123           The cathode was fabricated by depositing Cu onto a cut piece of expanded  
124 polytetrafluoroethylene (ePTFE) (Sterlitech). The ePTFE was pretreated by first performing an  
125 RCA cleaning process. The ePTFE was first treated with a mixture of H<sub>2</sub>O:HCl:H<sub>2</sub>O<sub>2</sub> (5:1:1) at  
126 80°C for 2 minutes, then a mixture of H<sub>2</sub>O:NH<sub>4</sub>OH:H<sub>2</sub>O<sub>2</sub> (5:1:1) for 2 minutes. After rinsing and  
127 drying, Cu was deposited onto the ePTFE via e-beam physical vapor deposition at a rate of 2 Å  
128 per second to a total thickness of 275 nm. The electrode was allowed to cool for 25 minutes before  
129 being removed from the chamber. The deposition thickness was confirmed using a test silicon  
130 wafer and cross-sectional SEM (spell out) characterization. The catalysts were then characterized  
131 via SEM (Figure S6), XPS (Figure S7), XRD (Figure S8), PEIS (Figure S9), and ECSA (Figure  
132 S10).



### 133 **Electrochemical Experiments with Temperature Measurement**

134           For the experiments where temperature was measured, a temperature probe (Omega  
135 Engineering) was submerged within the electrolyte as close to the surface of the cathode before  
136 cell assembly. Electrolysis occurred for each current density for 10 minutes or until steady-state  
137 was reached. Real-time temperature measurements were recorded and analyzed to capture heating  
138 during electrolysis. CO<sub>2</sub> (99.999%, Industrial Gas) and N<sub>2</sub> gas (99.999%, Industrial Gas) were  
139 provided for CO<sub>2</sub>R and HER measurements, respectively. The resistive heating of the cell is  
140 estimated through HER, as no buffer reactions occur without inlet CO<sub>2</sub>.

## 141 **Calculations for Cathodic Energy Efficiency**

142 Cathodic energy efficiency for a CO<sub>2</sub>-reduced product is defined as:

$$143 \quad EE (\%) = \frac{1.23 - E_0}{1.23 - E_{applied}} * FE (\%) \quad (1)$$

144 Where 1.23 V represents the thermodynamic potential for the oxygen evolution reaction (OER) at  
145 the anode,  $E_0$  is the thermodynamic potential for each product,  $E_{applied}$  is the applied potential vs  
146 RHE, and  $FE (\%)$  is the Faradaic efficiency towards that product.

## 147 **Modeling of AM Electrochemical System**

148 A steady-state mass-transport model is used in this work to estimate the local CO<sub>2</sub>  
 149 concentration. The one-dimensional model accounts for homogeneous reactions occurring for four  
 150 species (CO<sub>2</sub>, OH<sup>-</sup>, HCO<sub>3</sub><sup>-</sup>, and CO<sub>3</sub><sup>2-</sup>), diffusion of reactants and products, and electrochemical  
 151 source terms for the rate of consumption of CO<sub>2</sub> and production of OH<sup>-</sup>. This model, based on  
 152 previous CO<sub>2</sub>RR studies<sup>3-6</sup>, assumes that under alkaline conditions, the two major homogenous  
 153 reactions are as follows:



156 The resulting governing equations are as follows:

$$157 \quad 0 = D_{eff} D_{CO_2} \frac{\partial^2 [CO_2]}{\partial x^2} - k_{1f} [CO_2] [OH^-] + k_{1r} [HCO_3^-] - R_{CO_2} \quad (4)$$

$$158 \quad 0 = D_{eff} D_{OH^-} \frac{\partial^2 [OH^-]}{\partial x^2} - k_{1f} [CO_2] [OH^-] + k_{1r} [HCO_3^-] - k_{2f} [HCO_3^-] [OH^-] + k_{2r} [CO_3^{2-}] + R_{OH^-}$$

$$159 \quad (5)$$

$$160 \quad 0 = D_{eff} D_{HCO_3^-} \frac{\partial^2 [HCO_3^-]}{\partial x^2} - k_{1f} [CO_2] [OH^-] - k_{1r} [HCO_3^-] - k_{2f} [HCO_3^-] [OH^-] + k_{2r} [CO_3^{2-}]$$

$$161 \quad (6)$$

$$162 \quad 0 = D_{eff} D_{CO_3^{2-}} \frac{\partial^2 [CO_3^{2-}]}{\partial x^2} + k_{2f} [HCO_3^-] [OH^-] - k_{2r} [CO_3^{2-}] \quad (7)$$

163 where the electrochemical source terms take the following form:

$$164 \quad R_{CO_2} = \frac{j}{FL} \sum_i \frac{FE_i n_i}{z_i} \quad (8)$$

$$165 \quad R_{OH^-} = \frac{j}{FL} \sum_i \frac{FE_i m_i}{z_i} \quad (9)$$

166 In Equation 7 and 8,  $j$  represents the current density,  $F$  represents Faraday's constant,  $L$  represents  
167 the length of the catalyst layer (275 nm),  $n_i$  and  $m_i$  represent the stoichiometric coefficients for the  
168  $\text{CO}_2\text{RR}$  and hydroxide formation products, respectively,  $z_i$  represents the number of electrons for  
169 product  $i$ , and  $\text{FE}$  represents the product Faradaic efficiency. Faradaic efficiencies are applied from  
170 the experimental values. The model assumes that the charge transfer reactions occur  
171 homogeneously within the catalyst layer.

172 Dirichlet boundary conditions set to equilibrium values for all species are enforced at the  
173 exit. At the inlet,  $\text{CO}_2$  concentration is set assuming 100% gaseous  $\text{CO}_2$  and maximum solubility  
174 using Henry's law (34.1 mM). No-flux boundary conditions are used for all other species at the  
175 inlet. Direct simulations of the governing equations are performed using the finite volume CFD  
176 toolbox OpenFOAM second-order accuracy. Mesh convergence was confirmed, with a minimum  
177 grid resolution of 20 nm in the catalyst layer.

178 For modeling ethanol production in the reactor, a simplified model of the electrochemical  
179 cell comprising just the fluid dynamics and ethanol production based on experimental results were  
180 simulated in COMSOL. Ethanol was generated at the surface of the electrode at  $110 \text{ nmol s}^{-1} \text{ cm}^{-2}$   
181 and was coupled with the laminar fluid flow field through the reactor geometry to drive  
182 convective and diffusive transport.

183 We modeled the resistive heating in COMSOL Multiphysics using the heat transfer physics  
184 package. The heat generation across the domain was calculated as  $I^2R$ , where  $I$  represents the total  
185 current and  $R$  is the resistance. We used a value of  $7.458 \text{ } \Omega \text{ cm}^{-1}$  for electrolyte resistivity after  
186 accounting for losses due to membrane. Liquid and gas flows for this model were at  $5 \text{ mL min}^{-1}$   
187 and  $10 \text{ mL min}^{-1}$ , respectively. The coupled physics interface was used to convect heat according  
188 to the fluid flow fields designed in our AM reactor. No thermal effects from electrode resistance

189 or homogenous reaction were included. Mesh convergence was determined by scaling the mesh  
190 size until peak temperature converged.

191 We define  $Da$  with respect to partial penetration, concentration of  $CO_2$  at the gas-liquid  
192 interface, and current density below:

$$193 \quad Da_{diff} = \frac{\tau_{DMI}}{[CO_2]_0 P / j} = \frac{P / D_{CO_2}}{[CO_2]_0 / m} \quad (10)$$

194 where  $m$  is the molar consumption from reduction ( $m = j/nF$ , where  $j$  is the current density),  $P$  is  
195 the liquid penetration depth into the ePTFE substrate,  $D_{CO_2}$  is the diffusivity of  $CO_2$  in aqueous  
196 electrolyte, and  $[CO_2]_0$  is the concentration of  $CO_2$  at the gas-liquid interface. Using this equation,  
197 we perform a diffusion timescale analysis to solicit a regime diagram for transport in the GDE.  
198 Figure S22 shows that this rescaling results in all profiles collapsing onto a single curve, which  
199 identifies  $Da$  as one of the relevant non-dimensional parameters to quantify mass transport  
200 limitations to the catalyst surface.

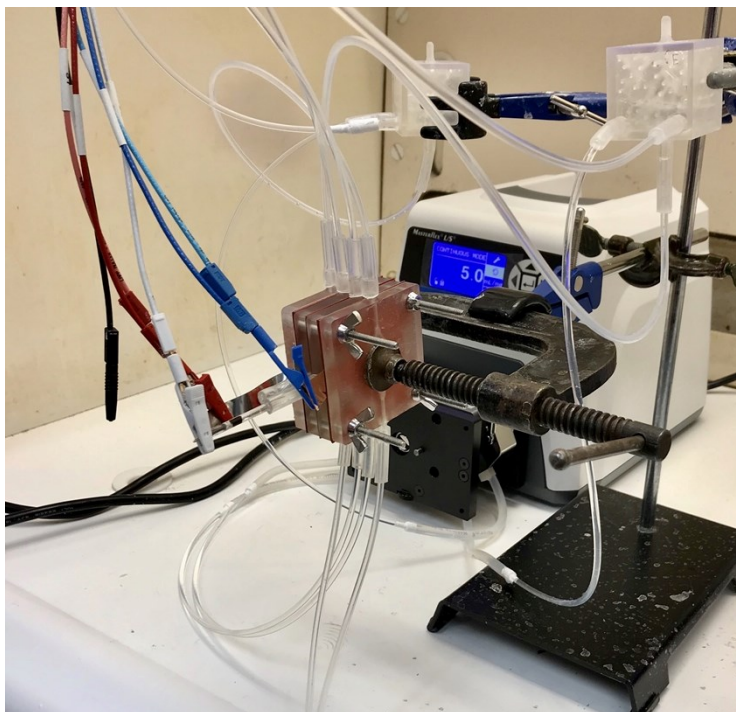
## 201 **Calculations for Product Yield**

202 Product yield is defined for an electrochemical CO<sub>2</sub>R process as:

$$203 \quad \text{Yield} = \frac{\text{products out}}{\text{reactants in}} = \frac{\text{mol } C_xH_yO_z \text{ produced}}{\text{mol } CO_2 \text{ in}} \quad (11)$$

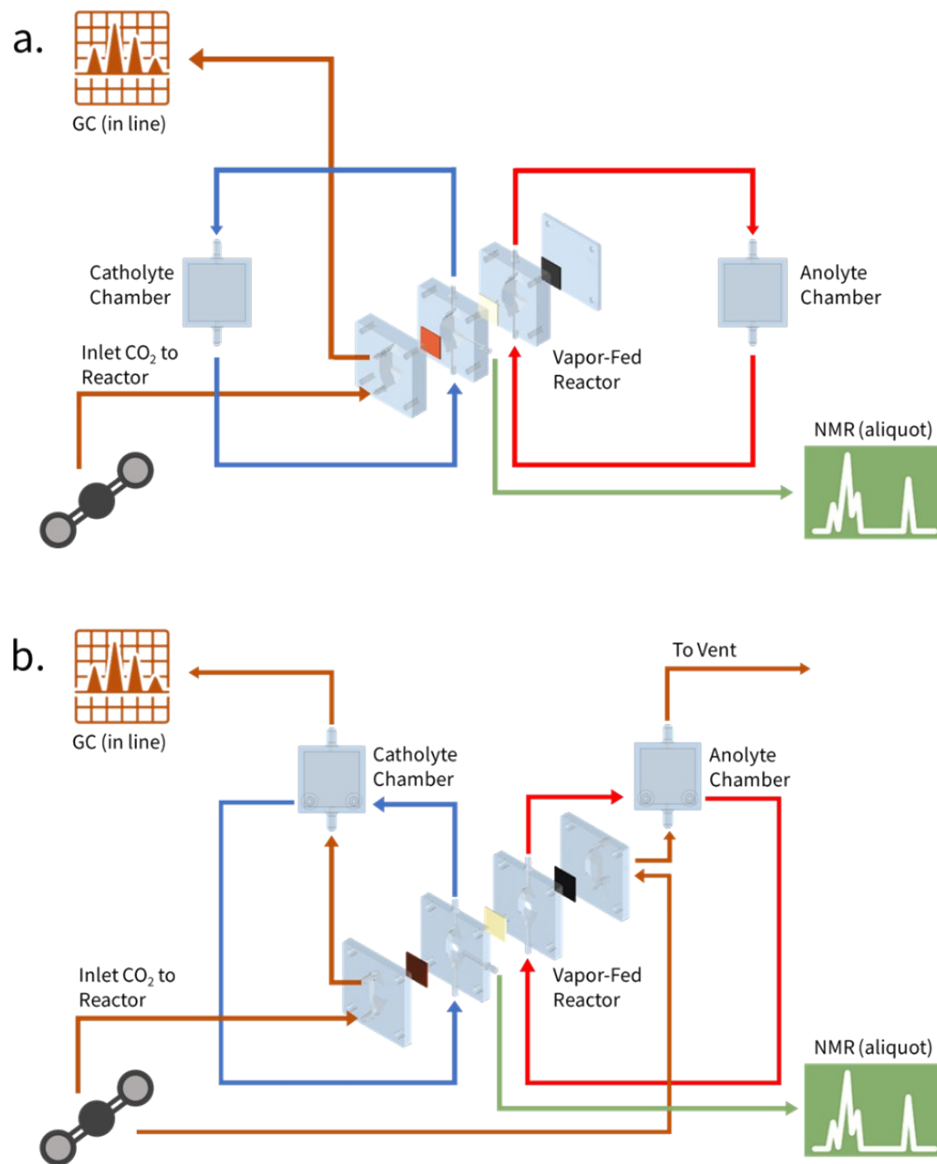
204 Yield is an important metric that must be considered, as it encompasses activity, selectivity and  
205 conversion. It is used in similar fields as the primary metric to evaluate the reactor performance;  
206 considering the differences in catalyst composition and reaction area, local electrolyte  
207 environment, and reactor and system design, we employ it here as a quantitative metric that can  
208 be used to compare results from many reports across the field. Table S10 contains parameters used  
209 for calculation including geometric surface area, inlet CO<sub>2</sub> flow rate, and partial current densities  
210 to calculate yield. Calculations assumed CO<sub>2</sub>R systems operated at room temperature.

## 211 Supplemental Figures



212

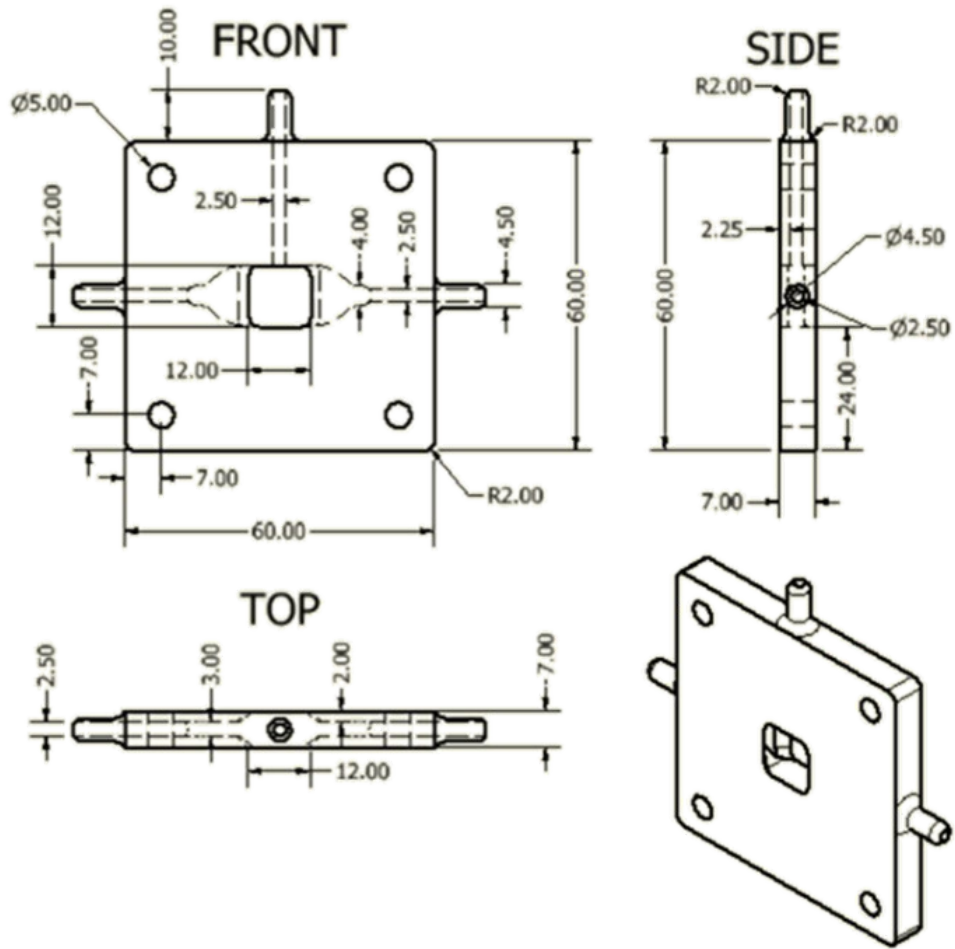
213 **Figure S1. Photograph of advanced manufactured reactor system during setup and pre-electrolysis.**



214

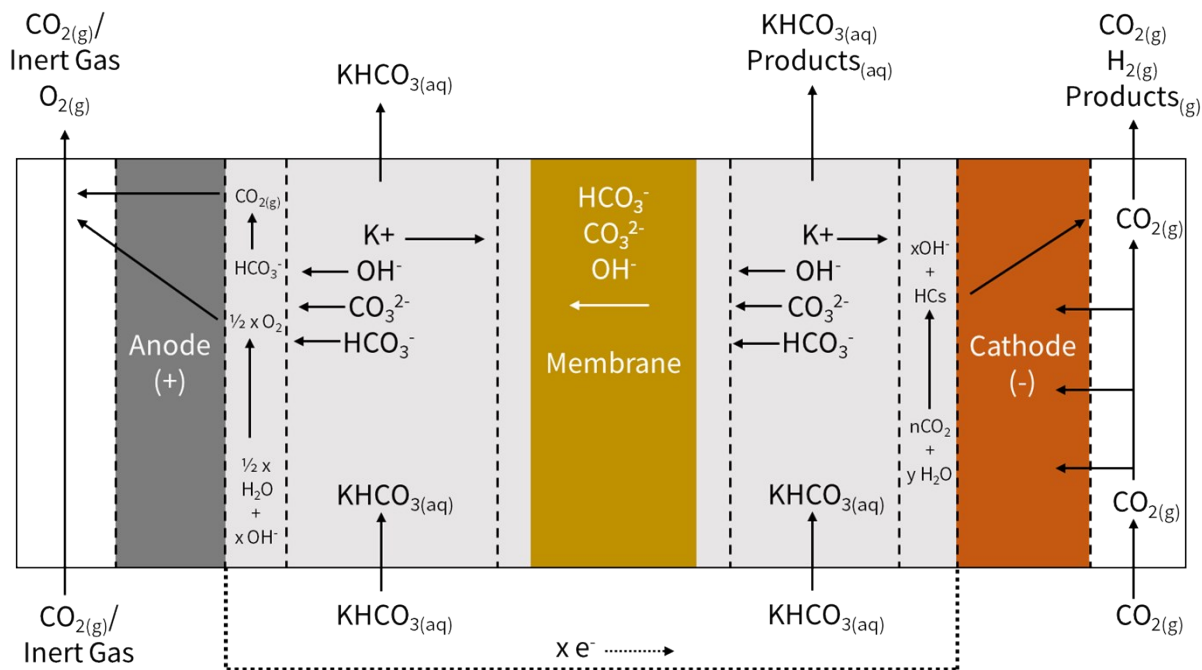
215 **Figure S2. Simplified system design for electrochemical CO<sub>2</sub> reduction experiments.** (a) System design for  
 216 Generations 1 & 2. (b) System design for Generation 3 experiments. Blue arrows indicate the catholyte flow direction,  
 217 red arrows indicate the anolyte flow direction, and orange arrows indicate the gas flow direction. Gas chromatography  
 218 (GC) samples are measured in real-time with the experiment. Electrolyte samples for NMR were recovered at the  
 219 conclusion of each experiment.





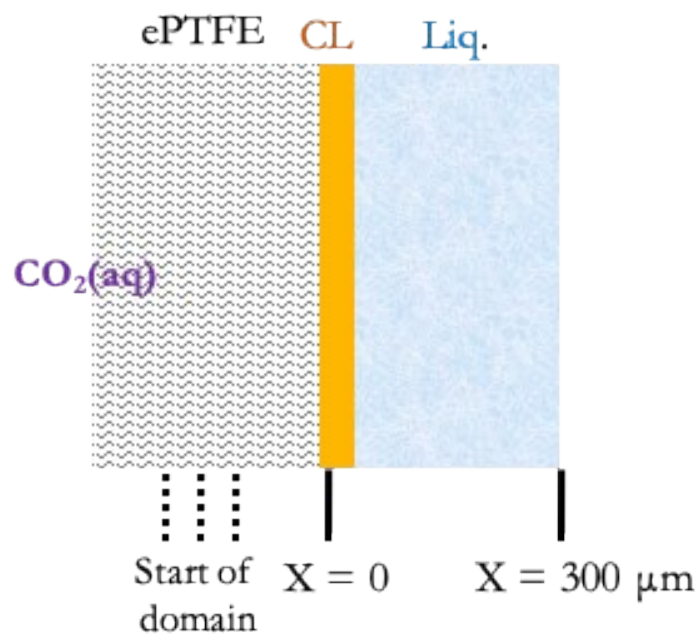
220

221 **Figure S3. Detailed drawing of Generation 3 Reactor.** Drawing and dimensions of catholyte chamber of the  
 222 Generation 3 reactor design. All dimensions are in millimeters.



223  
224

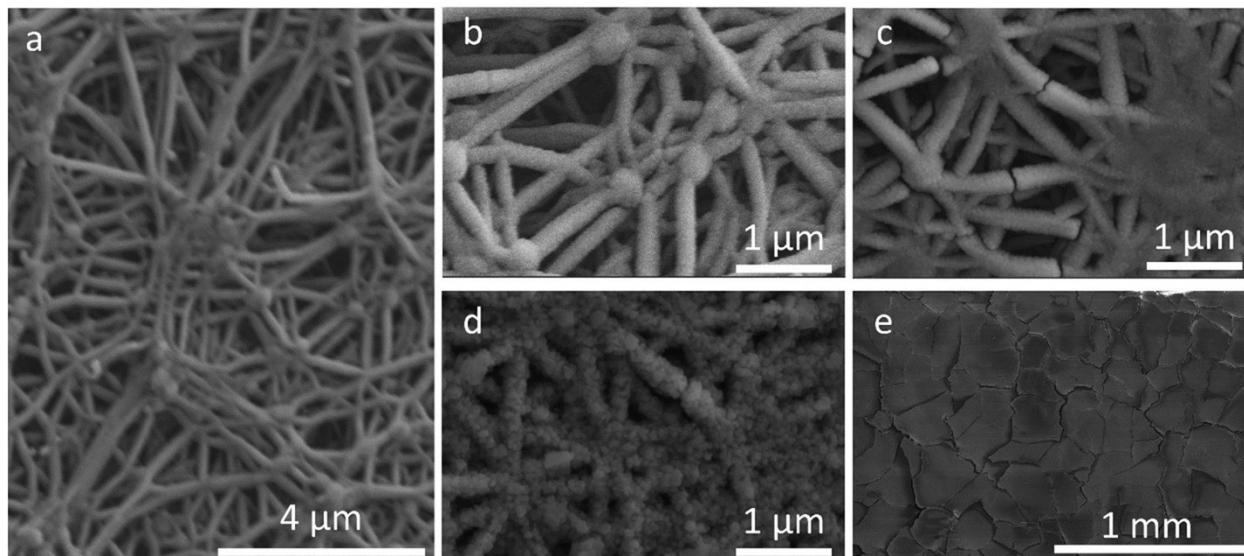
Figure S4. Schematic representation of the species transport in the Generation 3 reactor.



225

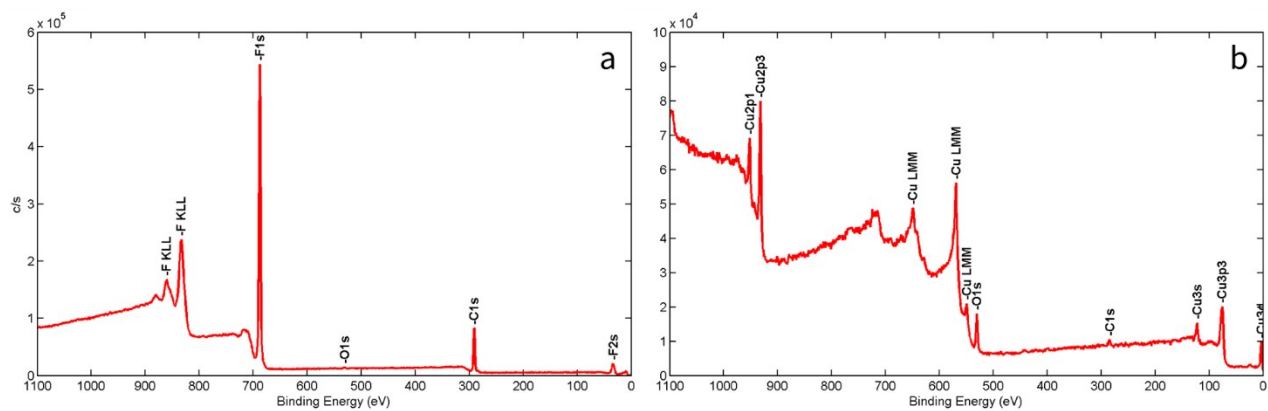
226 **Figure S5. Schematic representation of the computational domain.** Aqueous  $\text{CO}_2$  is introduced at the domain inlet.

227 The length of the penetration depth into the ePTFE is set by the distance between the domain inlet  $x=0$ .



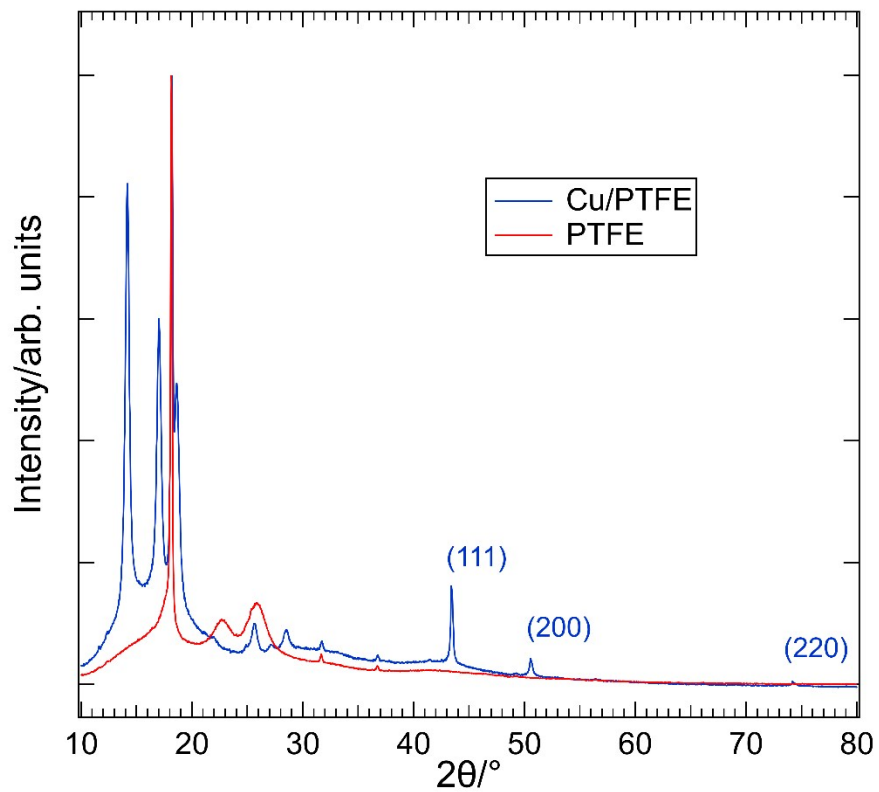
228

229 **Figure S6. SEM micrographs of Cu-catalyst coated expanded-PTFE.** (a) Pristine as-deposited copper catalyst and  
230 pore morphology. (b) Pristine catalyst with focus on PTFE-support nodes. (c) Pristine catalysts with nano-cracks along  
231 support filaments. Extensive mechanical deformation can extend cracking distribution. (d) Post-experiment catalyst,  
232 highlighting catalyst coarsening *in situ*. (e) Post-experiment catalyst with focus on micro-cracks that can form due to  
233 extensive mechanical deformation during handling.



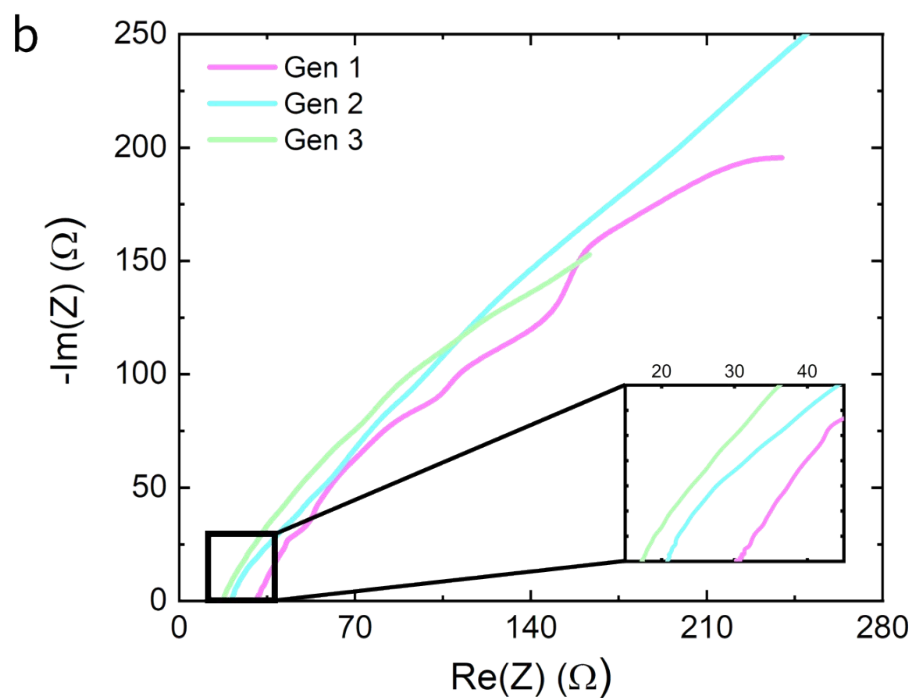
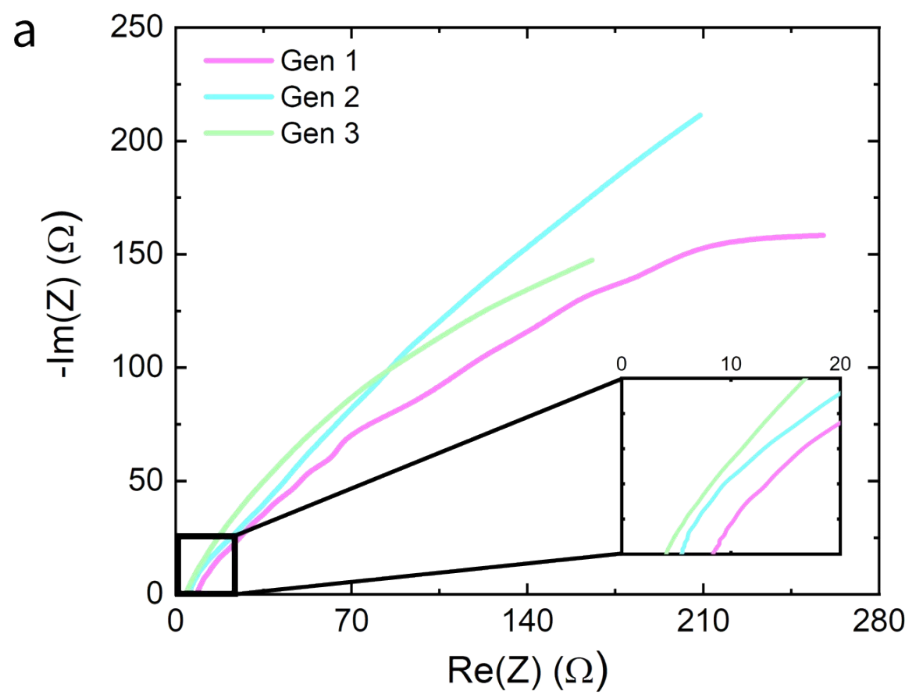
234

235 **Figure S7. X-ray photoemission spectroscopy (XPS).** (a) XPS of cleaned ePTFE. (b) XPS of Cu-deposited ePTFE. No metals  
 236 were detected on the ePTFE after cleaning, and only Cu was observed on the electrode surface after deposition.



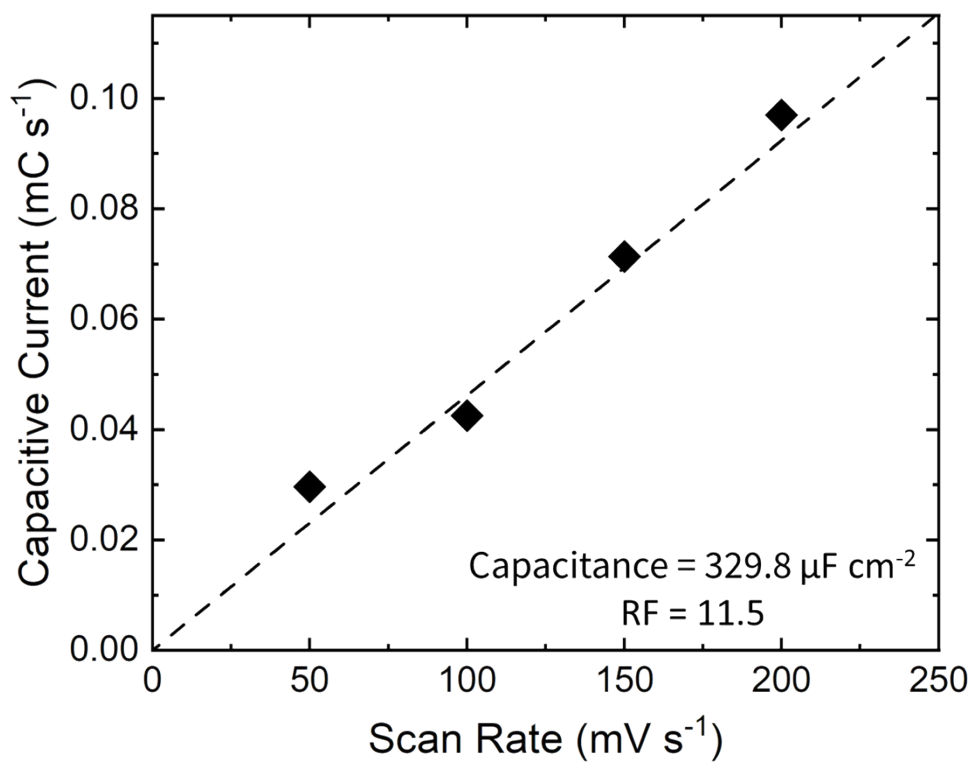
237

238 **Figure S8. X-ray diffraction (XRD).** XRD of ePTFE substrate and Cu-deposited ePTFE. Cu(111), Cu(200), and Cu(220)  
239 peaks were detected; no other facets were observed after deposition.



240

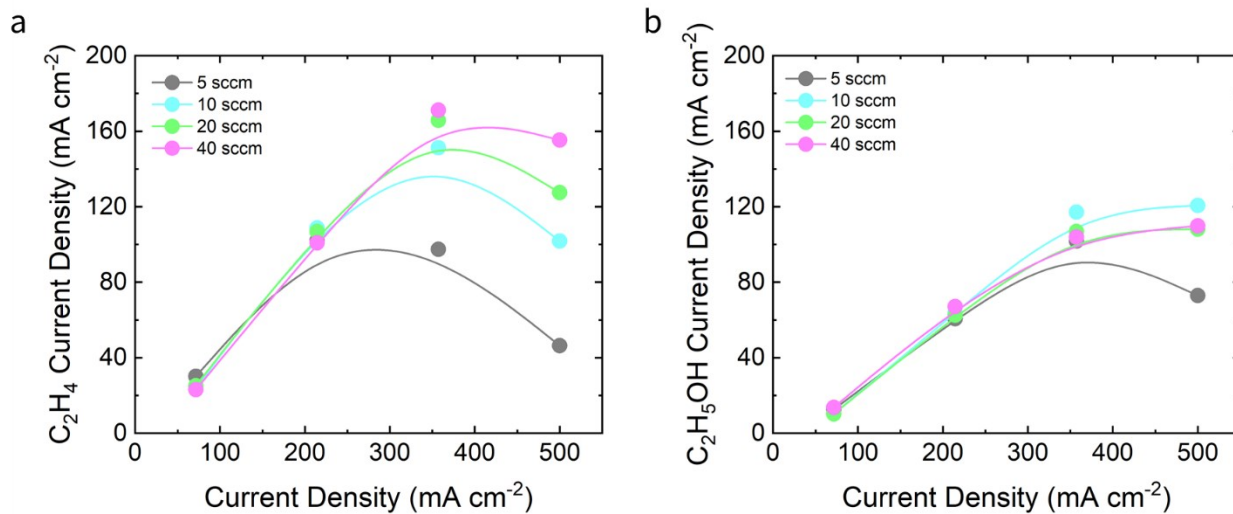
241 **Figure S9. PEIS for generations of reactors.** (a) Potentiostatic EIS for the half-cell (cathode to reference electrode) for all  
 242 three generations of reactors. (b) Potentiostatic EIS for the full-cell (cathode to anode) for all three generations of reactors.



243

244 **Figure S10. ECSA measurement of surface area.** Capacitance of Cu electrodes measured by cyclic voltammetry  
245 from 0.0 V to -0.1 V vs RHE.



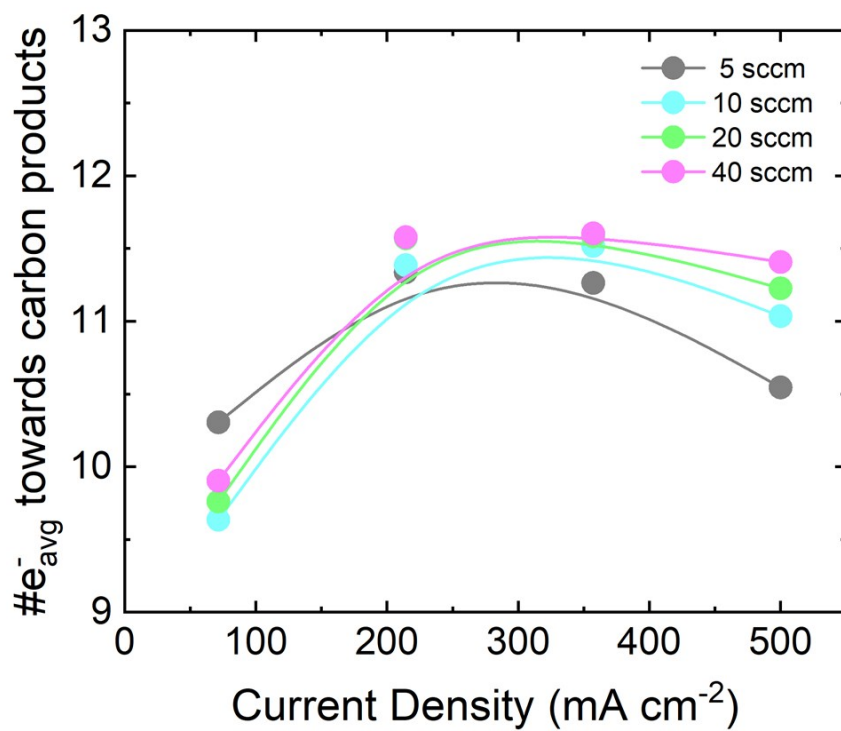


246

247

248 **Figure S11. Partial current densities (PCDs) of 2-carbon products for various inlet CO<sub>2</sub> flow rates.** (a) PCDs of

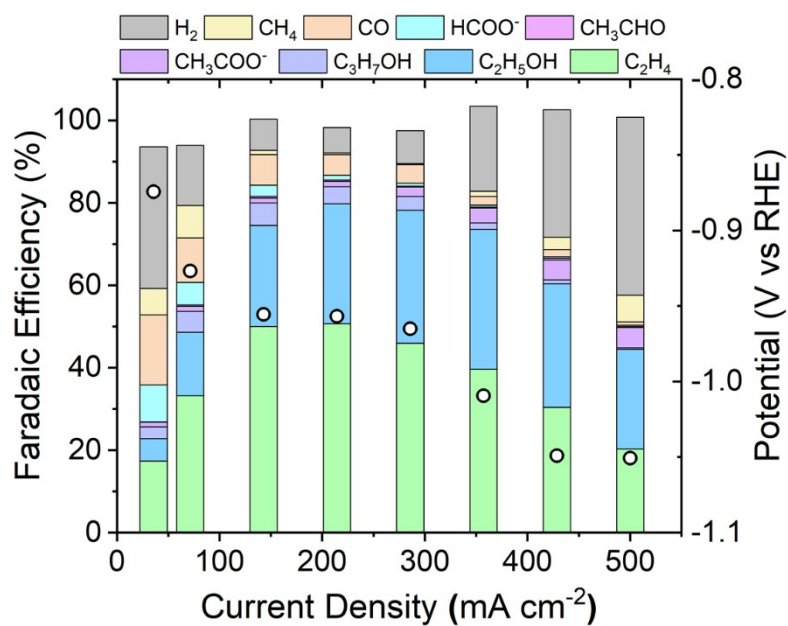
249 ethylene as a function of total current density. (b) PCDs of ethanol as a function of total current density.



250

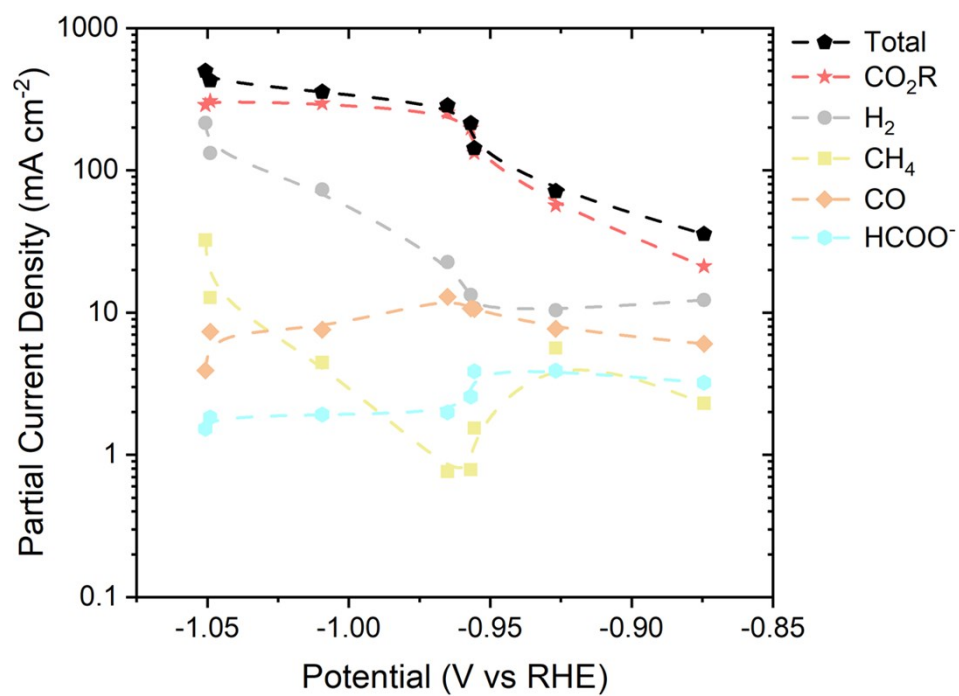
251

252 Figure S12. Average number of electrons transferred to CO<sub>2</sub>-reduced products.

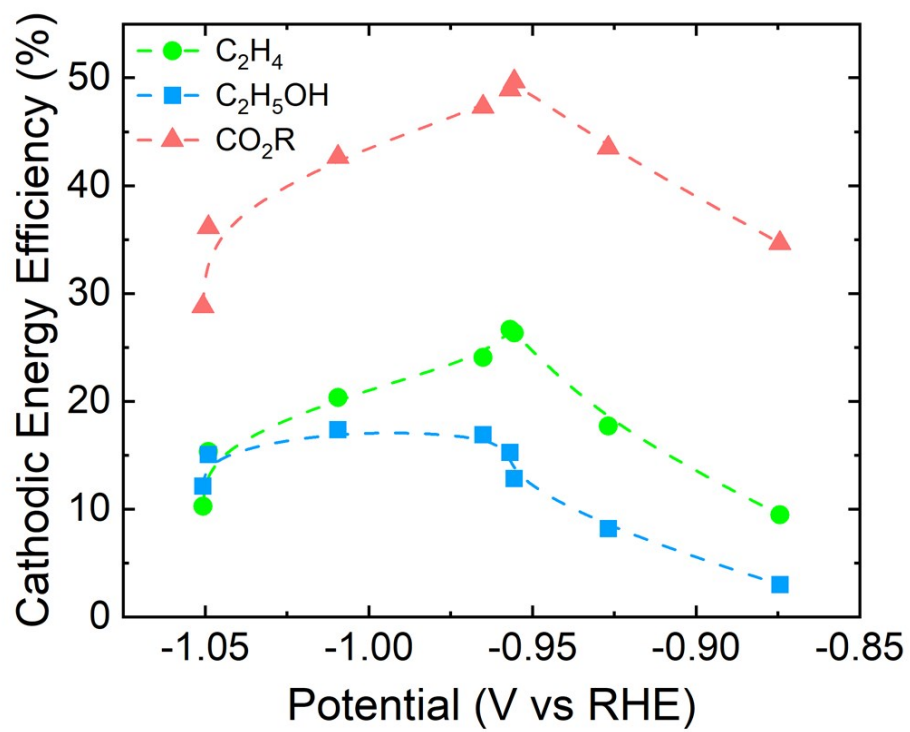


253  
254

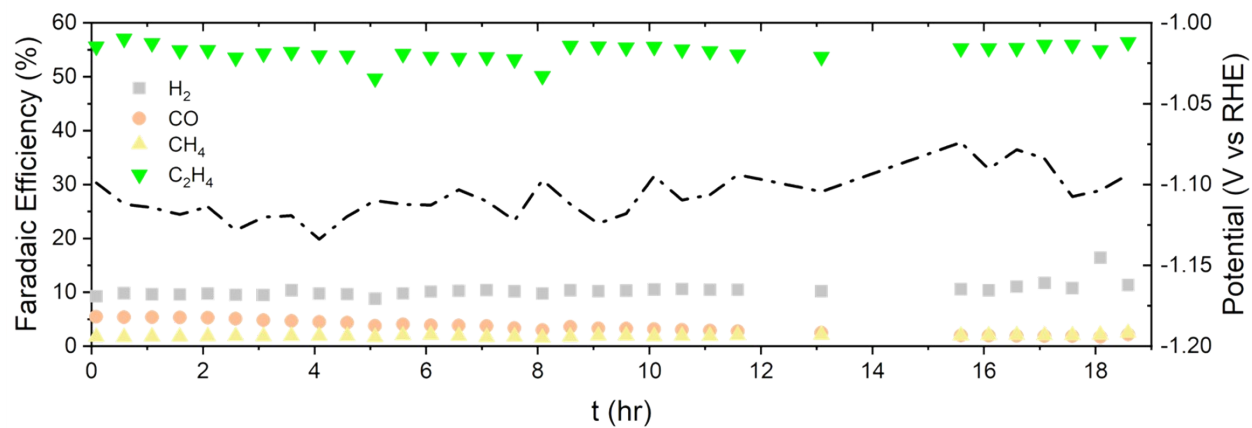
255 **Figure S13. Faradaic efficiencies and potential vs RHE as a function of geometric current density for 10 sccm.**  
256 FE for products formed is represented on the left axis; potential vs the reference hydrogen electrode (RHE) is  
257 represented on the right axis.



258  
 259 Figure S14. Partial current densities for hydrogen, single-carbon products, and CO<sub>2</sub>R as a function of potential  
 260 vs RHE at 10 sccm.



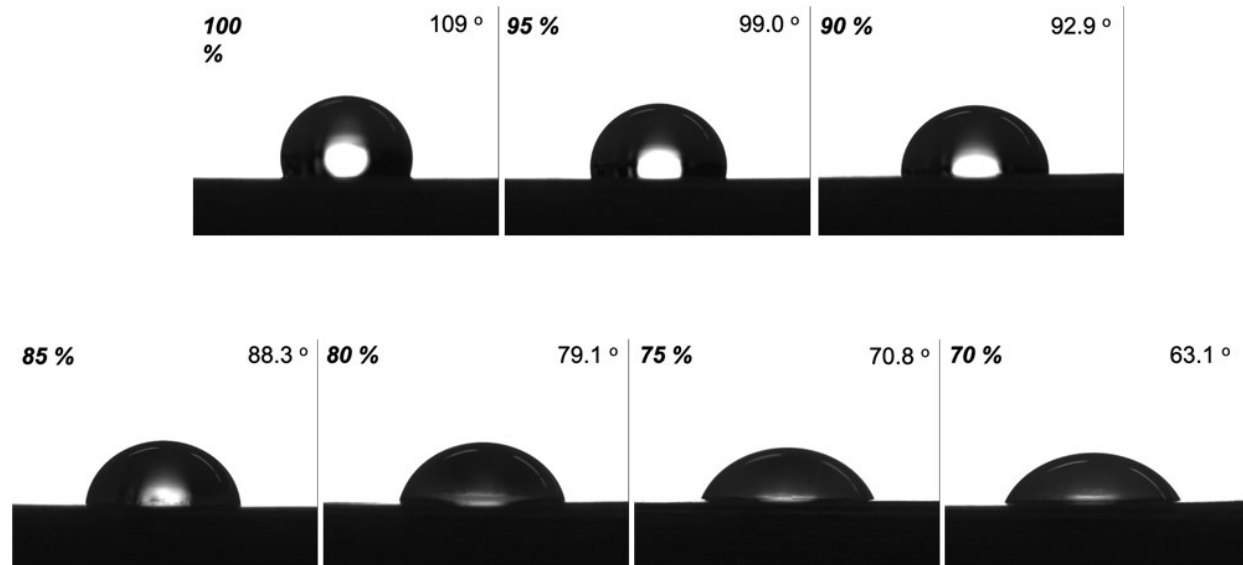
261  
262 Figure S15. Cathodic energy efficiency as function of potential vs RHE at 10 sccm.



263

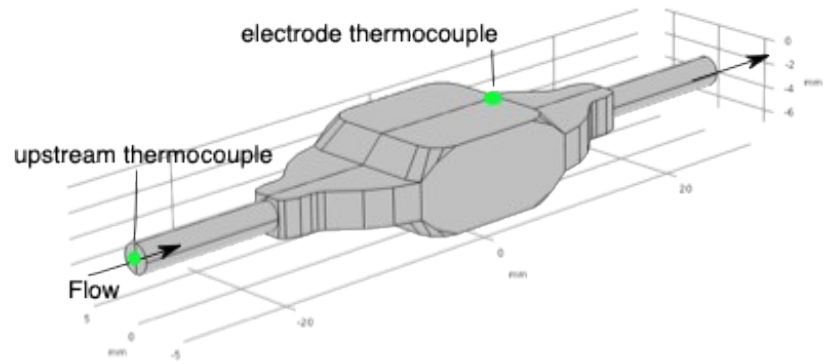
264 **Figure S16. Stability of performance of AM-VFR.** High selectivity (~55%) for C<sub>2</sub>H<sub>4</sub> was maintained for over 18  
 265 hours at 143 mA cm<sup>-2</sup>. Furthermore, selectivity to HER remained around 10% for the duration of the experiment.  
 266 Selectivity to CO and CH<sub>4</sub> also decreased to almost zero over the 18-hour experiment.

**Water content by mass (%)**



267  
268  
269  
270

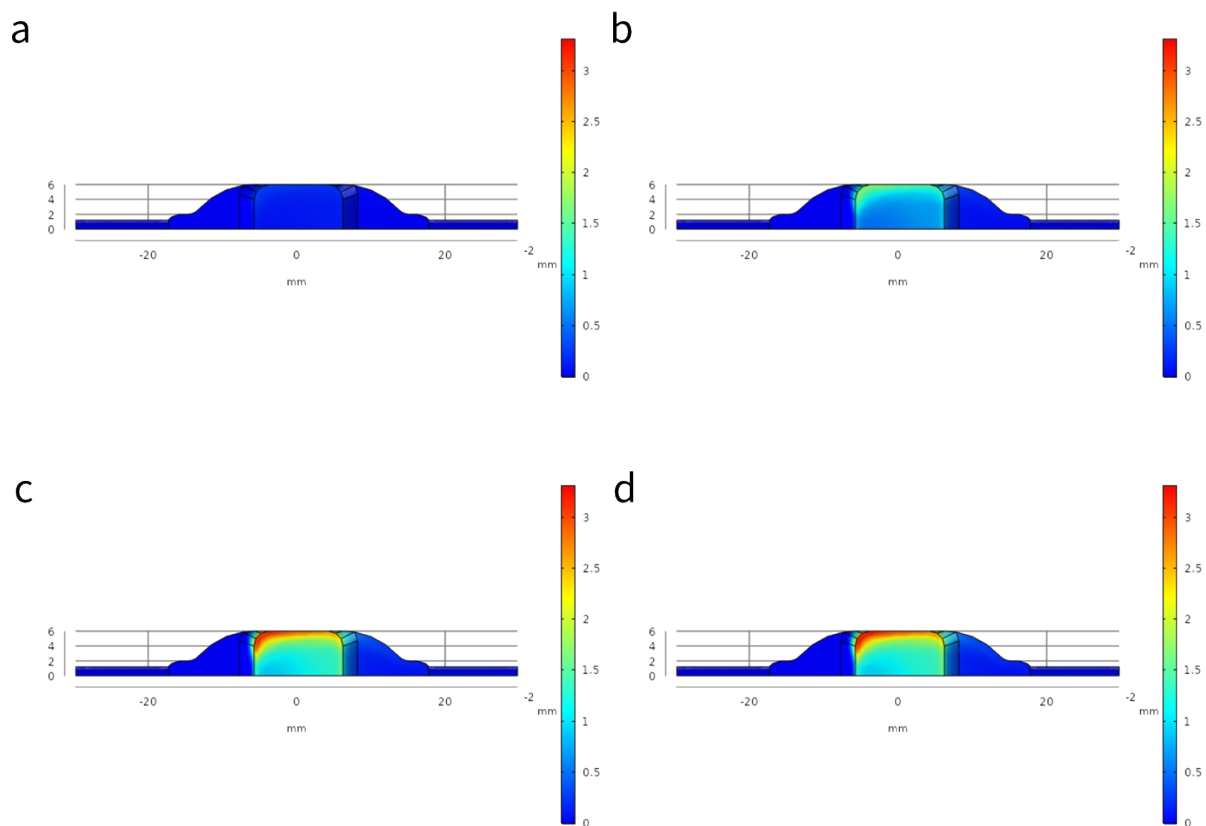
**Figure S17. Contact angle measurements.** Images of contact angle measurements for ethanol/water mixtures on bulk PTFE.



271

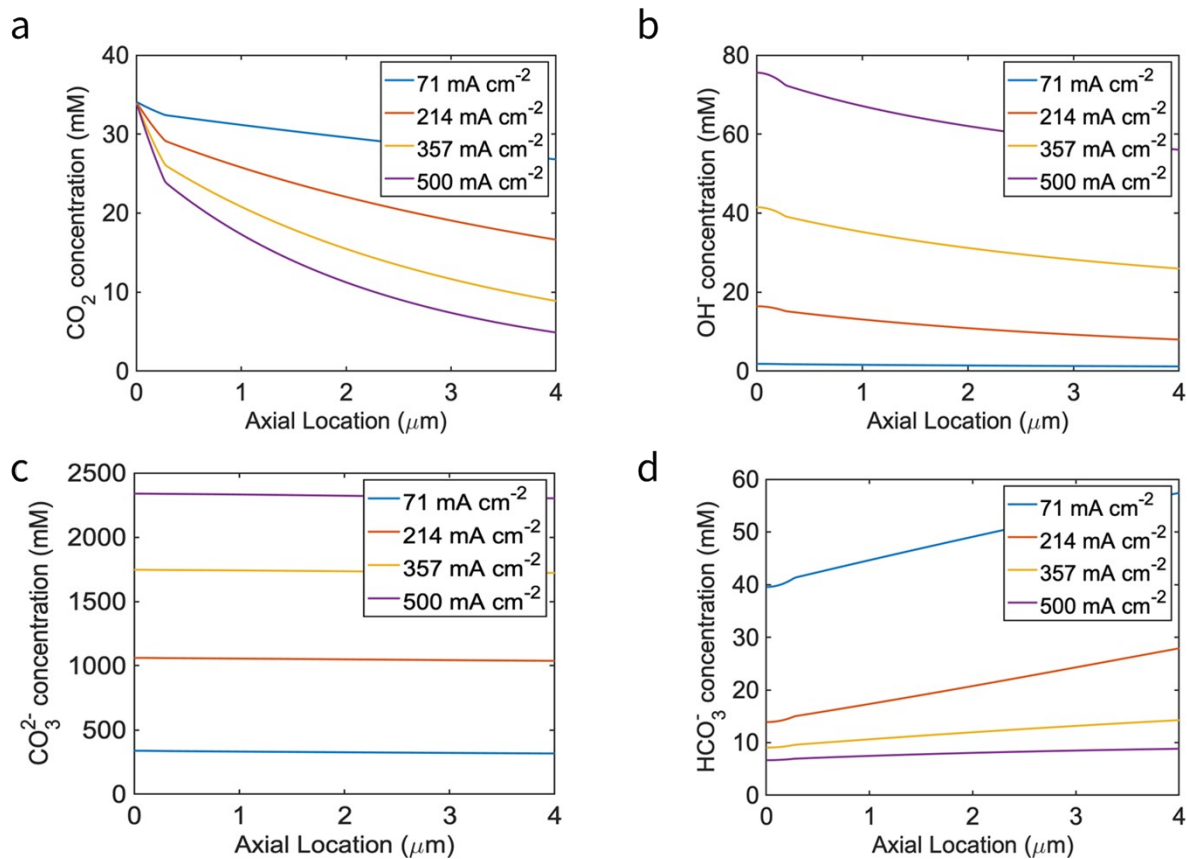
272 Figure S18. COMSOL model showing location of temperature probes during electrolysis.





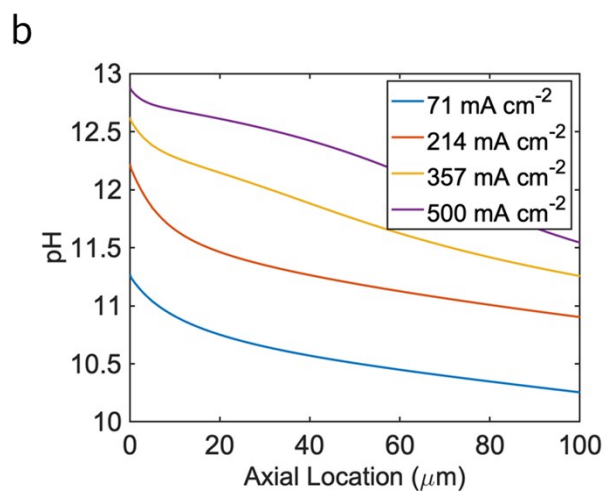
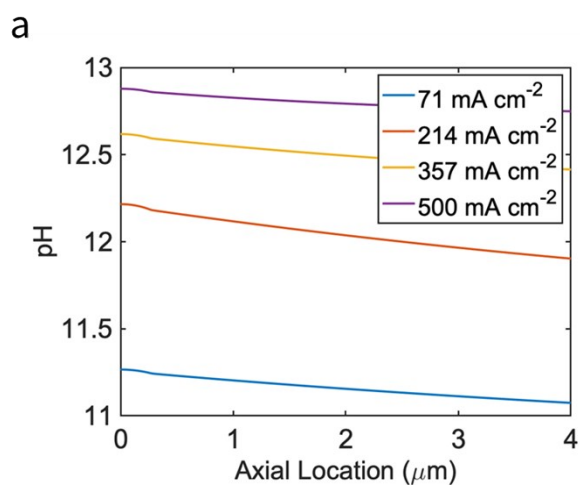
273

274 **Figure S19. Ethanol concentration profiles for 10 sccm CO<sub>2</sub> flow rate and 5 mL/min electrolyte flow rate for (a) 71**  
 275 **mA cm<sup>-2</sup> (b) 214 mA cm<sup>-2</sup> (c) 357 mA cm<sup>-2</sup> (d) 500 mA cm<sup>-2</sup>.**



276

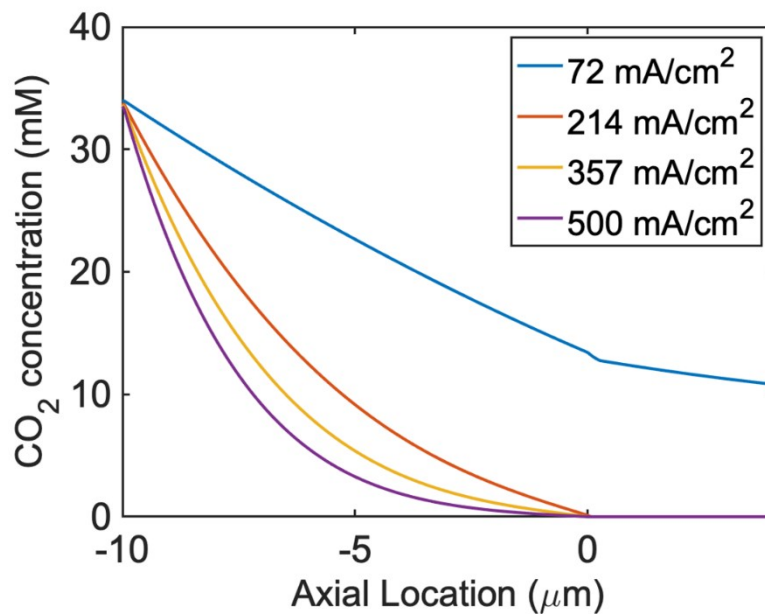
277 **Figure S20. Concentration profiles for species participating in homogenous reaction within aqueous electrolyte**  
 278 **for various current densities. (a) CO<sub>2</sub>. (b) OH<sup>-</sup>. (c) CO<sub>3</sub><sup>2-</sup>. (d) HCO<sub>3</sub><sup>-</sup>.**



279

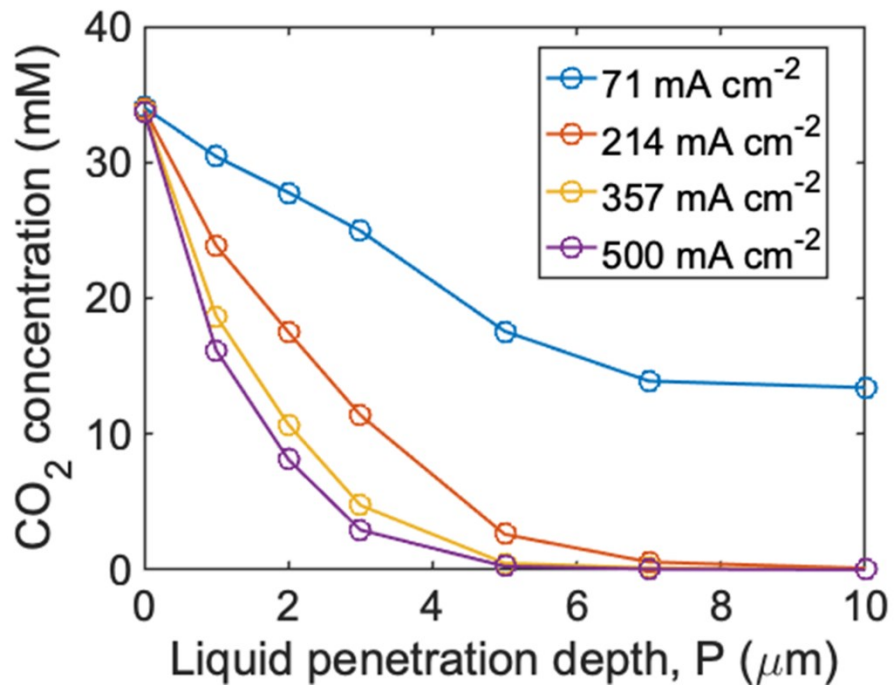
280 **Figure S21. pH profiles within aqueous electrolyte for various current densities. (a). 0-4  $\mu\text{m}$ . (b) 0-100  $\mu\text{m}$ .**

281



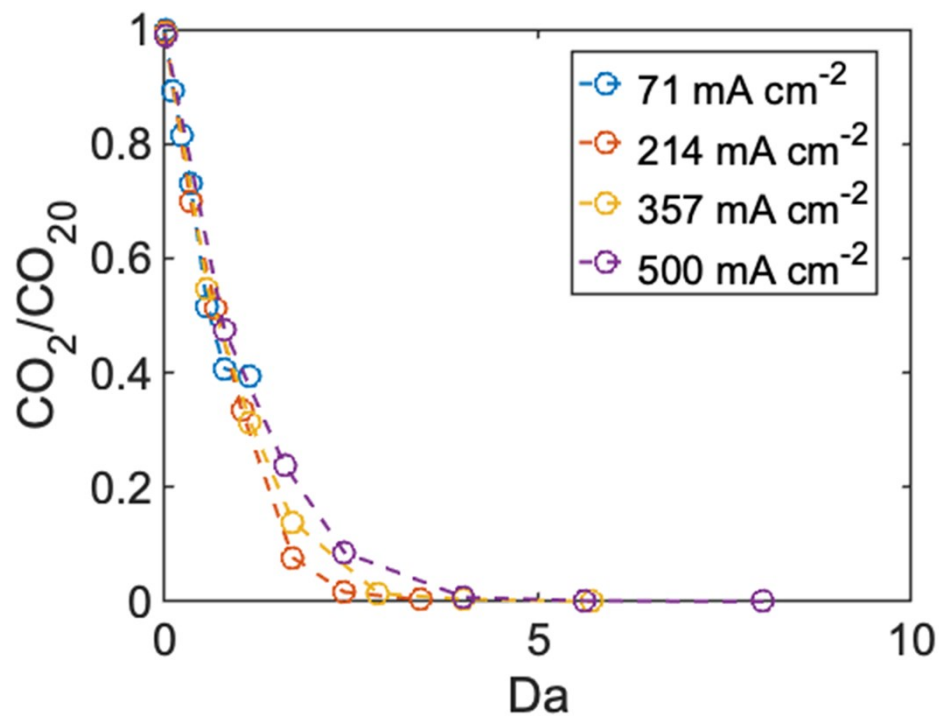
282

283 **Figure S22. CO<sub>2</sub> concentration profile for a subset of the domain around the catalyst layer.** Results correspond  
284 to the maximum penetration depth studied (10 μm) demonstrating complete depletion of the CO<sub>2</sub> before reaching the  
285 catalyst layer (x=0) for current densities above 100 mA/cm<sup>2</sup>.



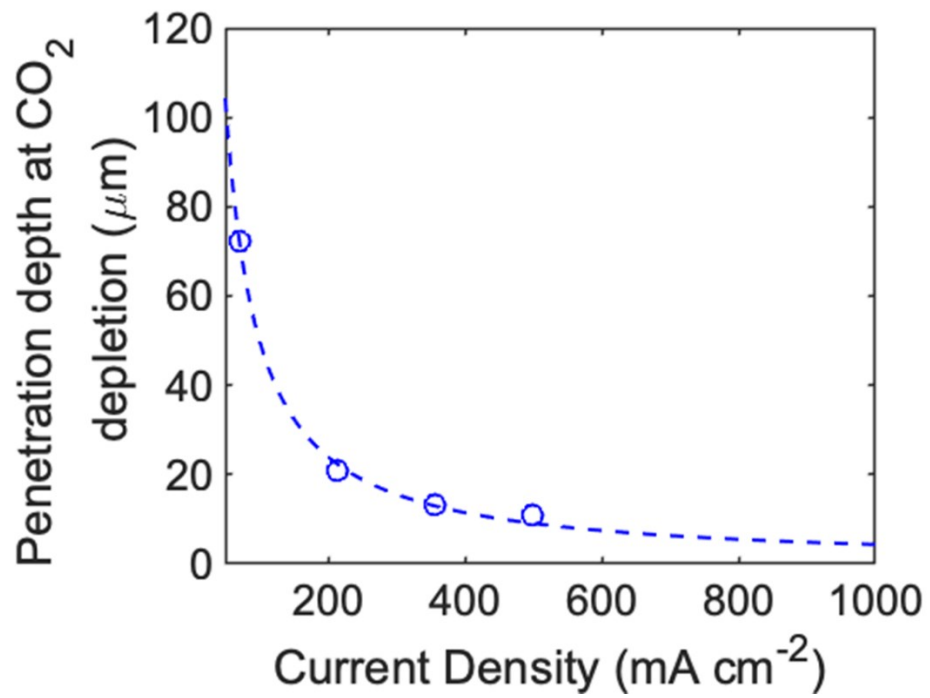
286  
287

288 Figure S23. CO<sub>2</sub> concentration as a function of liquid penetration depth into the diffusion media for various  
289 current densities.



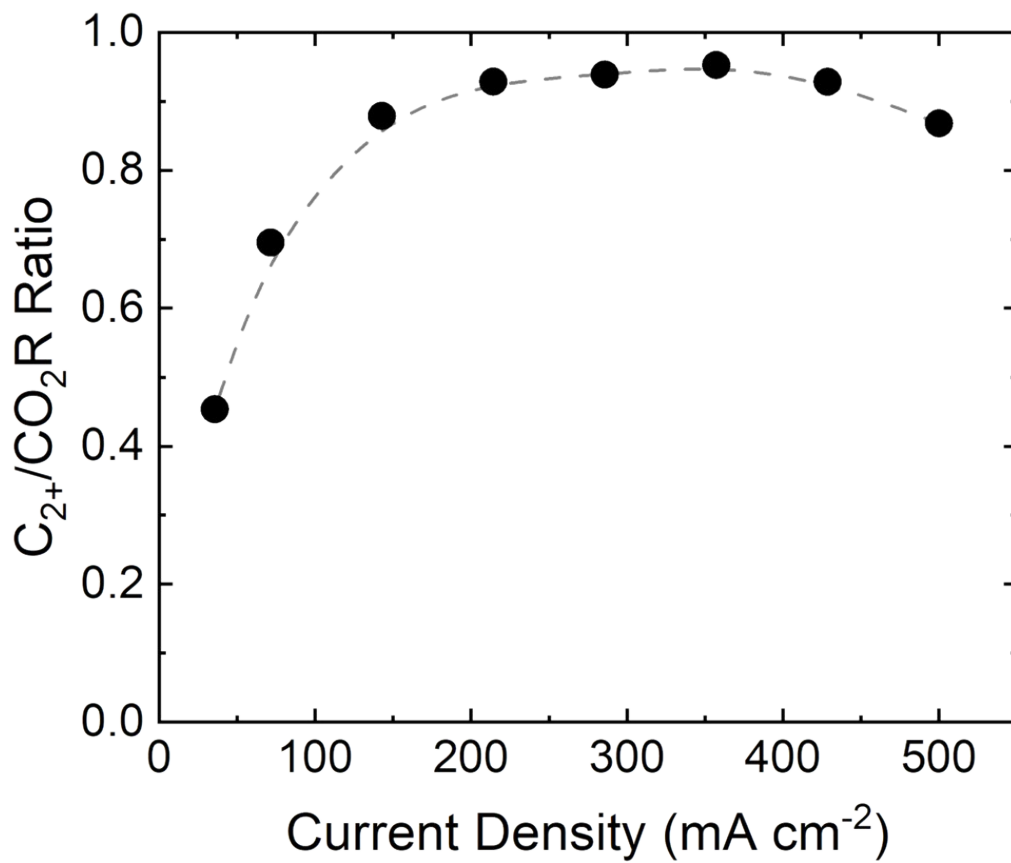
290

291 **Figure S24. Simulation results for CO<sub>2</sub> concentration at the CL at 10 sccm as a function of penetration depth**  
 292 **into the DM.** These results collapse when the data is represented as a function of Da, and non-dimensional CO<sub>2</sub>. This  
 293 identifies that the effects of current density and liquid penetration on the local CO<sub>2</sub> at the CL can be predicted by the  
 294 Da number.



295

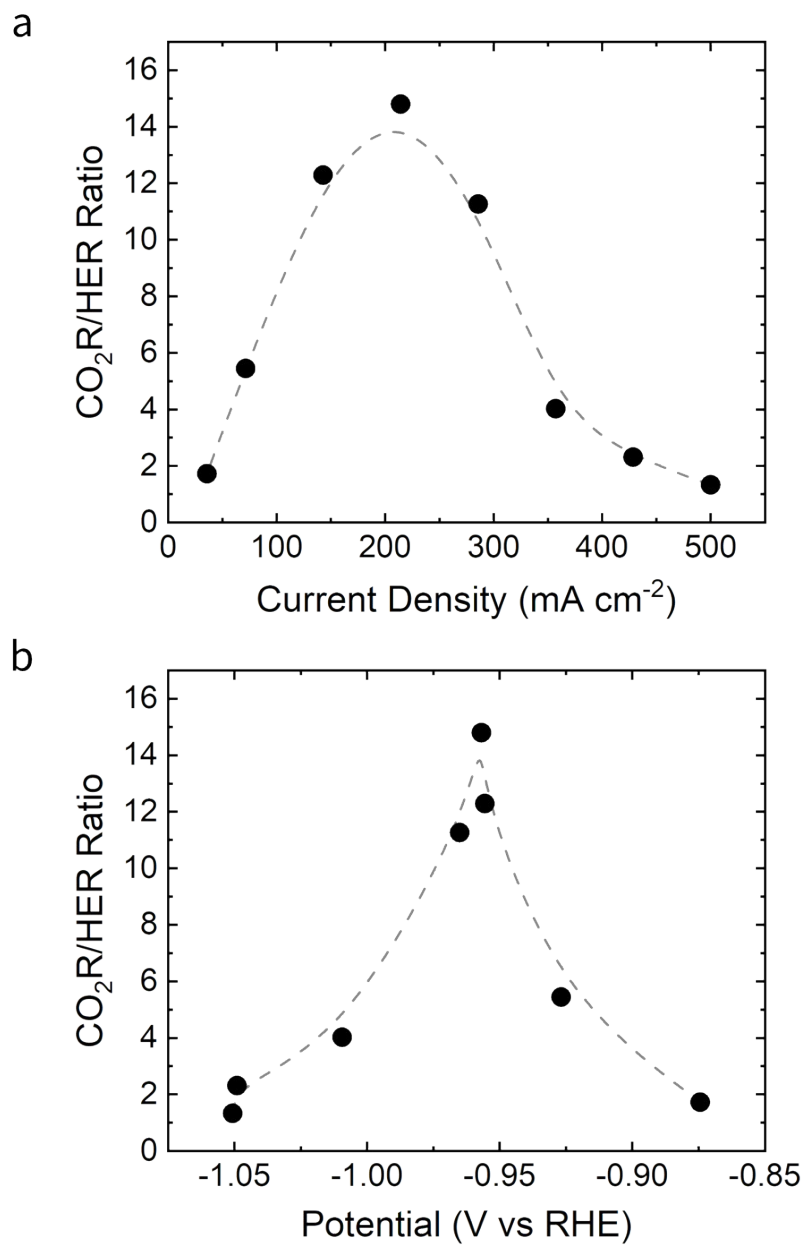
296 **Figure S25. CO<sub>2</sub> depletion at the inlet of the catalyst layer as a function of current density.** Depth of penetration  
297 at which CO<sub>2</sub> reaching the catalyst is zero.



298

299 **Figure S26. Measured fraction of CO<sub>2</sub>R current towards C<sub>2+</sub> products.** System shows high selectivity towards  
300 C<sub>2+</sub> past 100 mA cm<sup>-2</sup>.

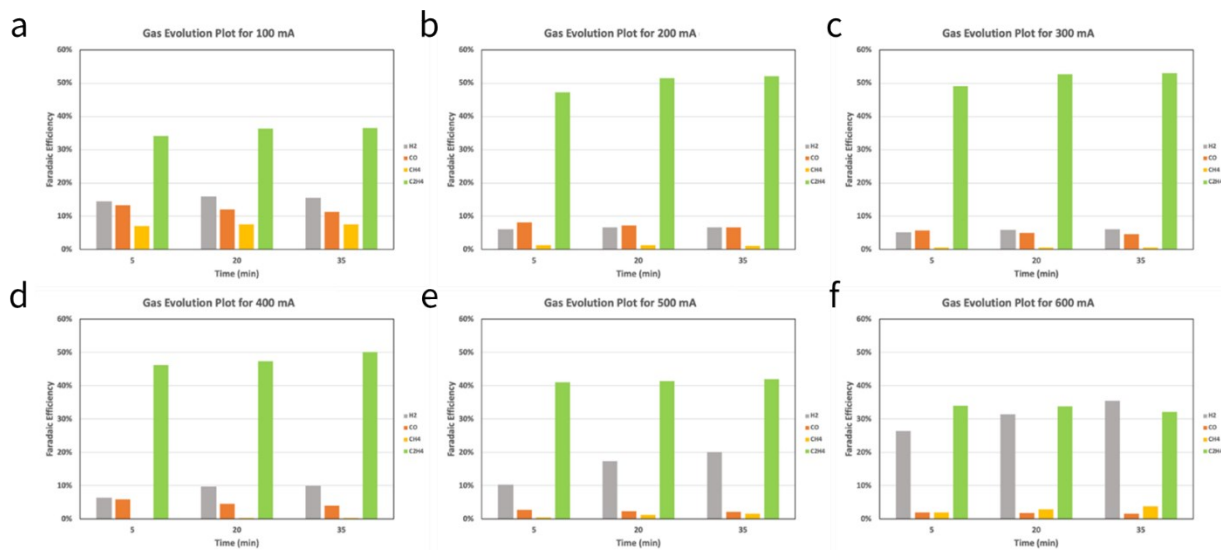




301

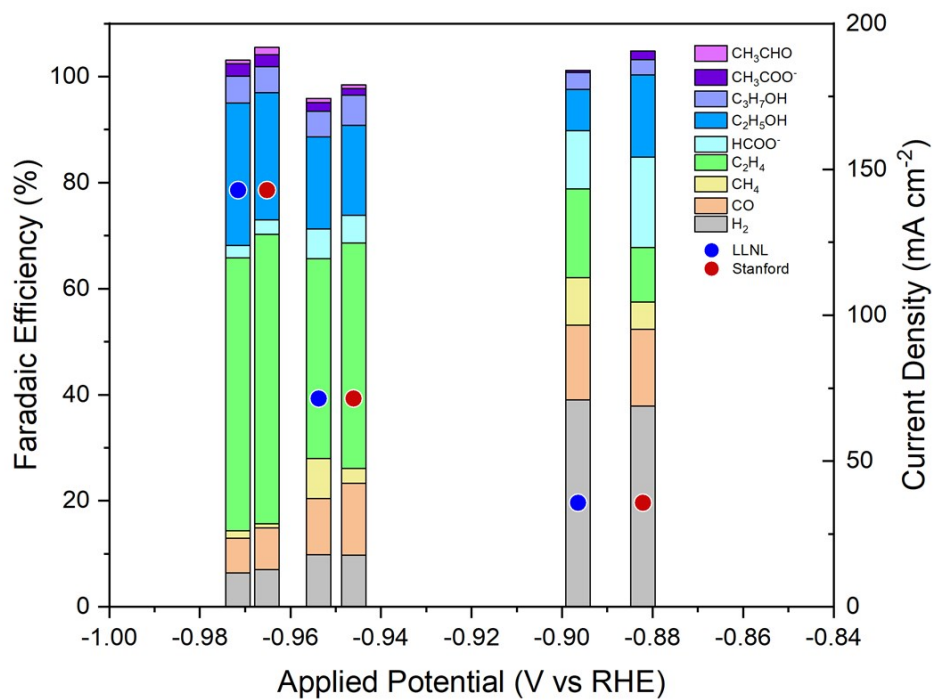
302 **Figure S27. Measured ratio of CO<sub>2</sub>R to HER.** Top shows the ratio as a function of current density (a) and  
303 corresponding potential (b). Peak occurs in tight potential window between -0.94 and -0.97 V vs RHE.

304



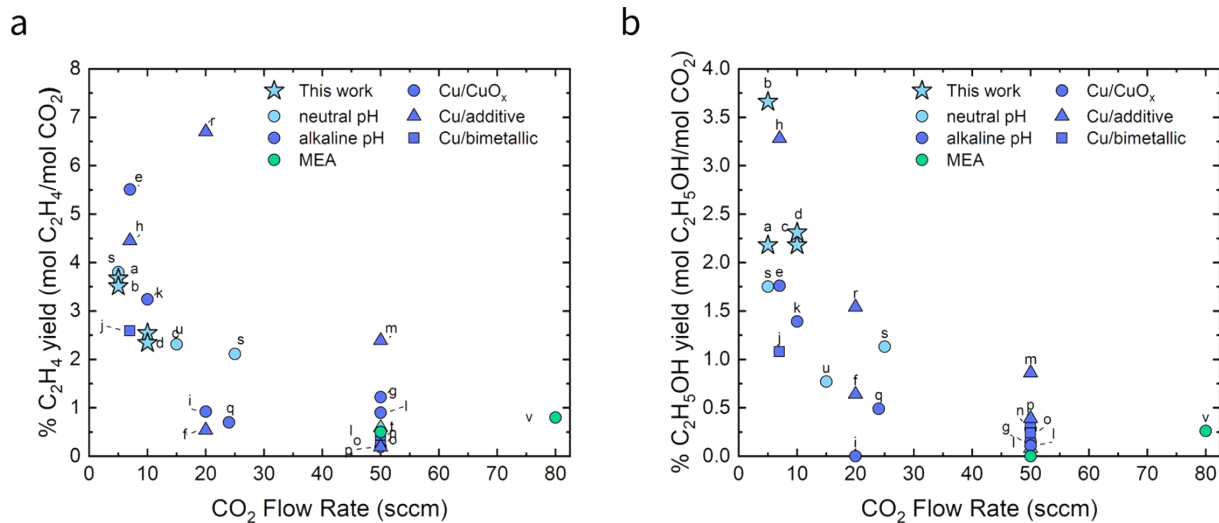
305

306 **Figure S28. Gas evolution of products over the course of the experiment.** Gas profiles are shown for (a) 100 mA.  
307 (b) 200 mA. (c) 300 mA. (d) 400 mA. (e) 500 mA. (f) 600 mA. Evolution of products is consistent throughout the  
308 experiments. Gas injections at 5 minutes were not included in Faradaic efficiency averages for gaseous products due  
309 to hydrogen increase.



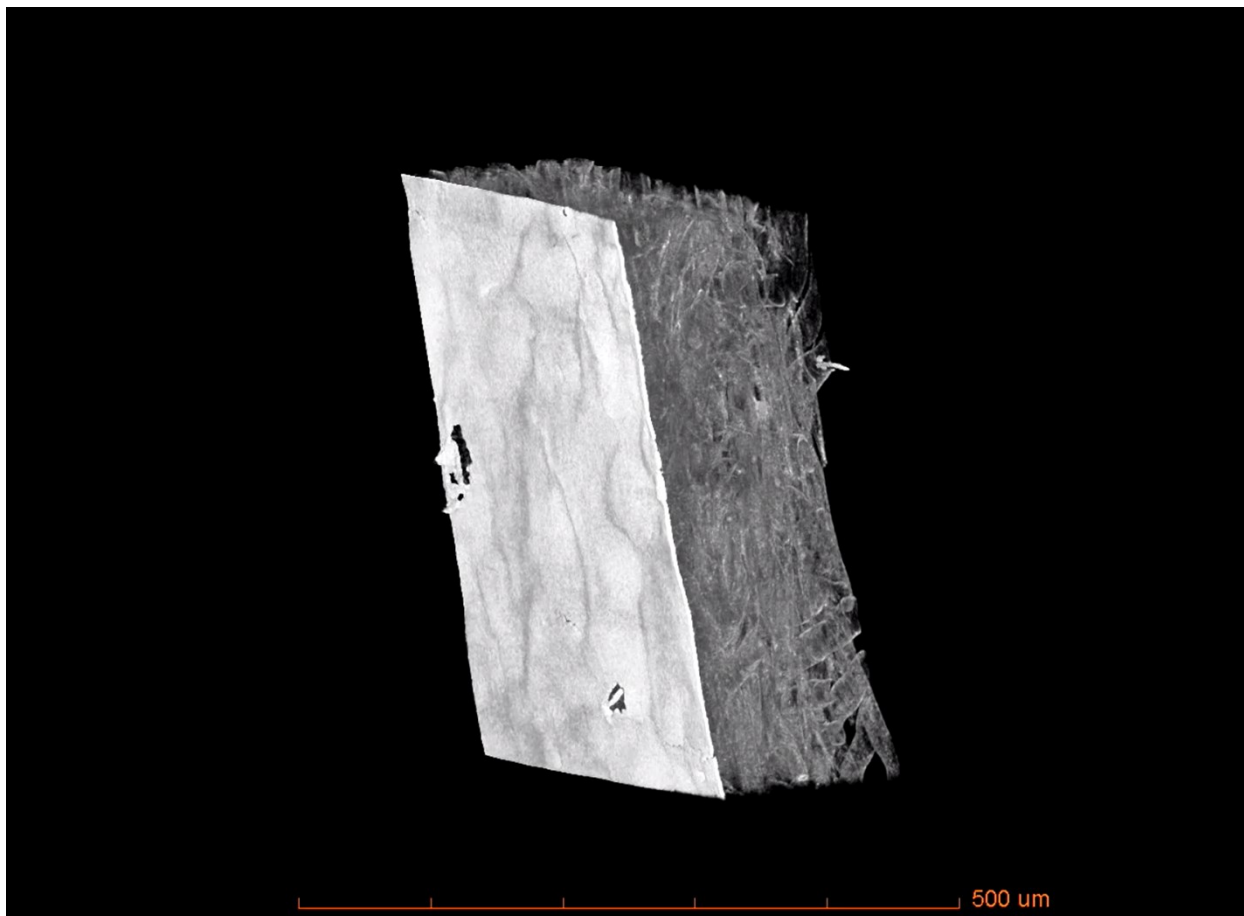
310

311 **Figure S29. Comparison of results performed at different sites.** Experiments performed at a workstation at Stanford  
 312 University (red) and Lawrence Livermore National Laboratory (blue) show similar results, indicating that the  
 313 performance of these reactors is reproducible and consistent.



314

315 **Figure S30. Comparison of literature for yield plots.** Comparison of literature and this work for (a) % ethylene and  
 316 (b) % ethanol yield as a function of inlet CO<sub>2</sub> flow rate. Data is colored to represent VFRs with bulk alkaline pH<sup>1,7-20</sup>,  
 317 bulk neutral pH<sup>3,16,21,22</sup>, and MEA<sup>13,23</sup> groupings. Point shapes represent catalyst layer composition class: Cu/Cu<sub>x</sub>, Cu  
 318 modified with a non-metal additive, and Cu-based bimetallics.



319  
320  
321

**Figure S31. X-ray Computed Tomography (XCT) of GDE.** See full .mp4 video attached for 360° rotating view of the substrate.

322 **Supplemental Tables**

Reaction Coefficient	Value
(1) $k_f$	$5.93 \times 10^3 M^{-1} s^{-1}$
(1) $k_r$	$1.34 \times 10^{-4} s^{-1}$
(2) $k_f$	$1.00 \times 10^8 M^{-1} s^{-1}$
(2) $k_r$	$2.15 \times 10^4 s^{-1}$

323 **Table S1. Forward and backward reaction coefficient values for Equations 1 and 2.**

Averages										
E (V vs RHE)	J (mA cm <sup>-2</sup> )	Ethylene	Ethanol	Propanol	Acetate	Acetaldehyde	Formate	Carbon Monoxide	Methane	Hydrogen
-1.091	500.000	9.278	14.593	0.000	3.741	0.225	0.220	0.442	7.631	47.587
-1.011	357.143	27.294	28.509	0.523	3.841	0.249	0.302	1.843	3.334	43.049
-1.003	214.286	47.587	28.326	2.814	2.601	0.223	1.081	4.392	1.014	15.398
-0.911	71.429	42.249	17.681	4.317	1.481	0.000	2.886	10.169	6.215	17.130

Table S2. Average values at 5 sccm CO<sub>2</sub> flow rate.

Standard Deviations										
E (V vs RHE)	J (mA cm <sup>-2</sup> )	Ethylene	Ethanol	Propanol	Acetate	Acetaldehyde	Formate	Carbon Monoxide	Methane	Hydrogen
0.054	-	0.473	1.201	0.000	0.834	0.319	0.171	0.087	0.667	4.062
0.012	-	3.578	6.051	0.065	0.752	0.062	0.089	0.541	1.138	0.456
0.003	-	1.837	0.876	1.453	0.420	0.052	0.424	2.234	0.516	3.196
0.012	-	1.026	9.278	0.781	0.330	0.000	0.361	0.908	4.600	1.578

Table S3. Standard deviation values at 5 sccm CO<sub>2</sub> flow rate.

Averages										
E (V vs RHE)	J (mA cm <sup>-2</sup> )	Ethylene	Ethanol	Propanol	Acetate	Acetaldehyde	Formate	Carbon Monoxide	Methane	Hydrogen
-1.051	500.00	20.365	24.130	0.372	4.950	0.179	0.306	0.784	6.493	43.219
-1.049	428.57	30.397	29.980	0.937	4.870	0.339	0.428	1.714	2.976	30.975
-1.005	357.14	39.620	33.952	1.609	3.576	0.190	0.538	2.124	1.249	20.597
-0.962	285.71	45.910	32.347	3.360	2.190	0.300	0.697	4.516	0.267	7.953
-0.955	214.29	50.693	29.094	4.128	1.307	0.333	1.199	4.989	0.368	6.225
-0.947	142.86	50.040	24.464	5.482	1.179	0.403	2.713	7.436	1.080	7.551
-0.922	71.43	33.201	15.418	5.066	1.253	0.285	5.480	10.791	7.902	14.571
-0.871	35.71	17.328	5.492	2.823	1.127	0.112	9.021	16.903	6.458	34.371

Table S4. Average values at 10 sccm CO<sub>2</sub> flow rate.

Standard Deviations										
E (V vs RHE)	J (mA cm <sup>-2</sup> )	Ethylene	Ethanol	Propanol	Acetate	Acetaldehyde	Formate	Carbon Monoxide	Methane	Hydrogen
0.013	-	1.568	3.943	0.078	1.111	0.069	0.101	0.187	2.100	7.598
0.021	-	2.699	0.721	0.142	0.281	0.111	0.061	0.118	0.809	4.084
0.013	-	4.804	2.250	0.438	0.569	0.086	0.053	0.697	0.297	5.516
0.006	-	3.070	0.561	0.196	0.039	0.079	0.078	0.753	0.032	0.661
0.004	-	0.751	2.733	0.762	0.364	0.110	0.121	1.144	0.085	0.840
0.015	-	1.529	2.844	0.298	0.381	0.111	1.084	1.365	0.385	1.762
0.008	-	2.085	1.926	0.153	0.977	0.076	1.022	2.730	0.400	1.704
0.006	-	5.173	2.786	1.559	0.935	0.193	6.730	1.114	0.997	0.530

Table S5. Standard deviation values at 10 sccm CO<sub>2</sub> flow rate.



Averages										
E (V vs RHE)	J (mA cm <sup>-2</sup> )	Ethylene	Ethanol	Propanol	Acetate	Acetaldehyde	Formate	Carbon Monoxide	Methane	Hydrogen
-1.061	500.000	25.506	21.625	0.368	4.138	0.218	0.240	0.925	4.297	36.389
-0.974	357.143	46.413	29.939	2.142	2.698	0.352	0.387	2.704	0.398	10.493
-0.976	214.286	49.862	29.154	3.298	1.944	0.130	0.922	3.182	0.610	7.320
-0.921	71.429	35.257	14.304	4.501	1.159	0.000	3.207	12.523	8.453	15.869

334

335

336

Table S6. Average values at 20 sccm CO<sub>2</sub> flow rate.

Standard Deviations										
E (V vs RHE)	J (mA cm <sup>-2</sup> )	Ethylene	Ethanol	Propanol	Acetate	Acetaldehyde	Formate	Carbon Monoxide	Methane	Hydrogen
0.005	-	0.155	0.303	0.026	0.097	0.019	0.008	0.129	0.138	0.726
0.003	-	3.598	4.355	0.505	0.458	0.085	0.086	0.149	0.070	0.005
0.038	-	3.426	9.165	0.578	1.111	0.183	0.112	1.048	0.068	3.238
0.002	-	2.588	1.514	1.101	0.106	0.000	0.147	0.413	1.652	2.984

337

338

Table S7. Standard deviation values at 20 sccm CO<sub>2</sub> flow rate.

Averages										
E (V vs RHE)	J (mA cm <sup>-2</sup> )	Ethylene	Ethanol	Propanol	Acetate	Acetaldehyde	Formate	Carbon Monoxide	Methane	Hydrogen
-1.070	500.000	31.068	21.971	0.488	3.239	0.253	0.233	1.012	3.103	31.582
-0.992	357.143	47.940	29.101	2.012	2.618	0.077	0.439	2.463	0.519	11.608
-0.989	214.286	47.078	31.334	3.832	2.601	0.478	1.362	2.540	0.718	8.021
-0.927	71.429	32.315	19.194	4.891	1.866	0.107	5.185	9.628	9.016	18.200

339

340

341

**Table S8. Average values at 40 sccm CO<sub>2</sub> flow rate.**

Standard Deviations										
E (V vs RHE)	J (mA cm <sup>-2</sup> )	Ethylene	Ethanol	Propanol	Acetate	Acetaldehyde	Formate	Carbon Monoxide	Methane	Hydrogen
0.009	-	2.637	1.615	0.035	1.185	0.076	0.035	0.018	0.832	2.383
0.025	-	2.450	4.249	0.798	0.850	0.109	0.146	1.078	0.396	3.145
0.029	-	5.507	9.406	0.590	0.907	0.299	0.273	0.708	0.216	1.755
0.000	-	0.137	4.055	0.032	0.664	0.151	1.475	1.524	1.890	0.582

342

343

344

**Table S9. Standard deviation values at 40 sccm CO<sub>2</sub> flow rate.**

345

Averages													
Generation	Average WE/RE Resistance ( $\Omega$ )	E (V vs RHE)	$J_{max}$ ( $\text{mA cm}^{-2}$ )	J ( $\text{mA cm}^{-2}$ )	Ethylene	Ethanol	Propanol	Acetate	Acetaldehyde	Formate	Carbon Monoxide	Methane	Hydrogen
1	7.595	-0.961	266.00	214.00	39.072	23.816	2.627	1.883	0.000	1.113	3.638	0.772	6.733
2	5.229	-1.002	298.00	214.00	35.523	25.204	1.789	2.088	0.000	0.994	1.055	1.185	12.526
3	3.494	-0.956	>500.00	214.00	50.536	29.944	4.456	1.228	0.362	1.200	5.254	0.371	5.827

346

**Table S10. Average values for reactor generation 1-3.**

347

348

Standard Deviations													
Generation	Average WE/RE Resistance ( $\Omega$ )	E (V vs RHE)	$J_{max}$ ( $\text{mA cm}^{-2}$ )	J ( $\text{mA cm}^{-2}$ )	Ethylene	Ethanol	Propanol	Acetate	Acetaldehyde	Formate	Carbon Monoxide	Methane	Hydrogen
1	0.463	0.014	-	-	1.725	0.118	0.520	0.353	0.000	0.208	0.671	0.796	1.623
2	0.195	0.005	-	-	2.047	3.359	0.185	0.299	0.000	0.273	0.179	0.188	0.141
3	0.212	0.004	-	-	0.835	2.619	0.476	0.403	0.115	0.149	1.242	0.103	0.333

349

**Table S11. Standard deviation values for reactor generations 1-3.**

Letter	CO <sub>2</sub> Flow Rate (sccm)	A <sub>geo</sub> (cm <sup>2</sup> )	Electrolyte	Partial Current Density (mA cm <sup>-2</sup> )		Molar Production Rate (mmol/hr)		Yield (mol product/mol CO <sub>2</sub> )		Reference
				C <sub>2</sub> H <sub>4</sub>	C <sub>2</sub> H <sub>5</sub> OH	C <sub>2</sub> H <sub>4</sub>	C <sub>2</sub> H <sub>5</sub> OH	C <sub>2</sub> H <sub>4</sub>	C <sub>2</sub> H <sub>5</sub> OH	
a	5	1.4	1M KHCO <sub>3</sub>	101.97	60.7	0.444	0.264	3.67%	2.18%	This work
b	5	1.4	1M KHCO <sub>3</sub>	97.48	101.82	0.424	0.443	3.51%	3.66%	This work
c	10	1.4	1M KHCO <sub>3</sub>	141.50	121.26	0.616	0.528	2.54%	2.18%	This work
d	10	1.4	1M KHCO <sub>3</sub>	130.27	128.49	0.567	0.559	2.34%	2.31%	This work
e	7	2	1M KOH	150	48	0.933	0.298	5.51%	1.76%	Ma et al. (2016)
f	20	1	1M KOH	84	100	0.261	0.311	0.54%	0.64%	Zhuang et al. (2018)
g	50	1	3.5M KOH + 5M KI	473	60	1.471	0.187	1.22%	0.15%	Dinh et al. (2018)
h	7	2.5	1M KOH	96.9	71.4	0.753	0.555	4.45%	3.28%	Hoang et al. (2017)
i	20	1	10M KOH	144	0	0.448	0.000	0.92%	0.00%	Wang et al. (2019)
j	7	0.785	1M KOH	180	75	0.439	0.183	2.59%	1.08%	Hoang et al. (2018)
k	10	1	1M KOH	252.1	108.4	0.784	0.337	3.24%	1.39%	Lv et al. (2018)
l	50	1	7M KOH	348.4	41.6	1.083	0.129	0.90%	0.11%	Wang et al. (2020)
m	50	1	7M KOH	930	336.5	2.892	1.046	2.39%	0.86%	Arquer et al. (2020)
n	50	1	1M KOH	135.8	128	0.422	0.398	0.35%	0.33%	Luo et al. (2019)
o	50	1	1M KOH	87.5	94	0.272	0.292	0.22%	0.24%	Li et al. (2019)
p	50	1	1M KOH	75	153	0.233	0.476	0.19%	0.39%	Wang et al. (2020)
q	24	1	2M KOH	130	92	0.404	0.286	0.70%	0.49%	Yang et al. (2020)
r	20	1	0.75M KOH	1043	240	3.243	0.746	6.70%	1.54%	Ma et al. (2020)
o	50	1	1M KHCO <sub>3</sub>	75	108	0.233	0.336	0.19%	0.28%	Li et al. (2019)
s	25	2	1M KHCO <sub>3</sub>	205	110	1.275	0.684	2.11%	1.13%	Tan et al. (2020)
s	5	2	1M KHCO <sub>3</sub>	74	34	0.460	0.211	3.80%	1.75%	Tan et al. (2020)
t	50	1	1M KHCO <sub>3</sub>	230	32	0.715	0.099	0.59%	0.08%	Li et al. (2020)
u	15	2	1M KHCO <sub>3</sub>	135	45	0.840	0.280	2.31%	0.77%	Ma et al. (2020)
l	50	1	0.15M KHCO <sub>3</sub>	195		0.606	0.000	0.50%	0.00%	Wang et al. (2020)
v	80	5	0.1M KHCO <sub>3</sub>	100	32	1.555	0.497	0.80%	0.26%	Garbardo et al. (2019)

350

351 **Table S12. Yield Comparison with literature.** Data is colored to represent VFRs with bulk alkaline pH<sup>1,7-19</sup>, bulk neutral pH<sup>3,16,21,22</sup>, and MEA<sup>13,23</sup> groupings.  
352 Point shapes represent catalyst layer composition class: Cu/Cu<sub>x</sub>, Cu modified with a non-metal additive, and Cu-based bimetallics.

## 353 References

- 354 1. Dinh, C.-T., Burdyny, T., Kibria, M.G., Seifitokaldani, A., Gabardo, C.M., de Arquer, F.P.G.,  
355 Kiani, A., Edwards, J.P., De Luna, P., Bushuyev, O.S., et al. (2018). CO<sub>2</sub> electroreduction to  
356 ethylene via hydroxide-mediated copper catalysis at an abrupt interface. *Science* *360*, 783–  
357 787.
- 358 2. Ma, S., Luo, R., Moniri, S., Lan, Y., and Kenis, P.J.A. (2014). Efficient Electrochemical Flow  
359 System with Improved Anode for the Conversion of CO<sub>2</sub> to CO. *J. Electrochem. Soc.* *161*,  
360 F1124–F1131.
- 361 3. Tan, Y.C., Lee, K.B., Song, H., and Oh, J. (2020). Modulating Local CO<sub>2</sub> Concentration as a  
362 General Strategy for Enhancing C- C Coupling in CO<sub>2</sub> Electroreduction. *Joule*.
- 363 4. Weng, L.-C., Bell, A.T., and Weber, A.Z. (2018). Modeling gas-diffusion electrodes for CO<sub>2</sub>  
364 reduction. *Phys. Chem. Chem. Phys.* *20*, 16973–16984.
- 365 5. Weng, L.-C., Bell, A.T., and Weber, A.Z. (2019). Towards membrane-electrode assembly  
366 systems for CO<sub>2</sub> reduction: a modeling study. *Energy Environ. Sci.*
- 367 6. Morales-Guio, C.G., Cave, E.R., Nitopi, S.A., Feaster, J.T., Wang, L., Kuhl, K.P., Jackson, A.,  
368 Johnson, N.C., Abram, D.N., Hatsukade, T., et al. (2018). Improved CO<sub>2</sub> reduction activity  
369 towards C<sub>2</sub>+ alcohols on a tandem gold on copper electrocatalyst. *Nat. Catal.* *1*, 764–771.
- 370 7. Ma, S., Sadakiyo, M., Luo, R., Heima, M., Yamauchi, M., and Kenis, P.J. (2016). One-step  
371 electrosynthesis of ethylene and ethanol from CO<sub>2</sub> in an alkaline electrolyzer. *J. Power*  
372 *Sources* *301*, 219–228.
- 373 8. Zhuang, T.-T., Liang, Z.-Q., Seifitokaldani, A., Li, Y., De Luna, P., Burdyny, T., Che, F.,  
374 Meng, F., Min, Y., Quintero-Bermudez, R., et al. (2018). Steering post-C–C coupling  
375 selectivity enables high efficiency electroreduction of carbon dioxide to multi-carbon alcohols.  
376 *Nat. Catal.* *1*, 421–428.
- 377 9. Hoang, T.T., Ma, S., Gold, J.I., Kenis, P.J., and Gewirth, A.A. (2017). Nanoporous copper  
378 films by additive-controlled electrodeposition: CO<sub>2</sub> reduction catalysis. *ACS Catal.* *7*, 3313–  
379 3321.
- 380 10. Wang, Y., Shen, H., Livi, K.J., Raciti, D., Zong, H., Gregg, J., Onadeko, M., Wan, Y.,  
381 Watson, A., and Wang, C. (2019). Copper Nanocubes for CO<sub>2</sub> Reduction in Gas Diffusion  
382 Electrodes. *Nano Lett.* *19*, 8461–8468.
- 383 11. Hoang, T.T., Verma, S., Ma, S., Fister, T.T., Timoshenko, J., Frenkel, A.I., Kenis, P.J., and  
384 Gewirth, A.A. (2018). Nanoporous Copper–Silver Alloys by Additive-Controlled  
385 Electrodeposition for the Selective Electroreduction of CO<sub>2</sub> to Ethylene and Ethanol. *J. Am.*  
386 *Chem. Soc.* *140*, 5791–5797.

- 387 12. Lv, J.-J., Jouny, M., Luc, W., Zhu, W., Zhu, J.-J., and Jiao, F. (2018). A highly porous copper  
388 electrocatalyst for carbon dioxide reduction. *Adv. Mater.* *30*, 1803111.
- 389 13. Wang, Y., Wang, Z., Dinh, C.-T., Li, J., Ozden, A., Kibria, M.G., Seifitokaldani, A., Tan, C.-  
390 S., Gabardo, C.M., Luo, M., et al. (2020). Catalyst synthesis under CO<sub>2</sub> electroreduction  
391 favours faceting and promotes renewable fuels electrosynthesis. *Nat. Catal.* *3*, 98–106.
- 392 14. de Arquer, F.P.G., Dinh, C.-T., Ozden, A., Wicks, J., McCallum, C., Kirmani, A.R., Nam,  
393 D.-H., Gabardo, C., Seifitokaldani, A., Wang, X., et al. (2020). CO<sub>2</sub> electrolysis to  
394 multicarbon products at activities greater than 1 A cm<sup>-2</sup>. *Science* *367*, 661–666.
- 395 15. Luo, M., Wang, Z., Li, Y.C., Li, J., Li, F., Lum, Y., Nam, D.-H., Chen, B., Wicks, J., Xu, A.,  
396 et al. (2019). Hydroxide promotes carbon dioxide electroreduction to ethanol on copper via  
397 tuning of adsorbed hydrogen. *Nat. Commun.* *10*, 1–7.
- 398 16. Li, Y.C., Wang, Z., Yuan, T., Nam, D.-H., Luo, M., Wicks, J., Chen, B., Li, J., Li, F., Garcia  
399 de Arquer, F.P., et al. (2019). Binding site diversity promotes CO<sub>2</sub> electroreduction to ethanol.  
400 *J. Am. Chem. Soc.*
- 401 17. Wang, X., Wang, Z., García de Arquer, F.P., Dinh, C.-T., Ozden, A., Li, Y.C., Nam, D.-H.,  
402 Li, J., Liu, Y.-S., Wicks, J., et al. (2020). Efficient electrically powered CO<sub>2</sub>-to-ethanol via  
403 suppression of deoxygenation. *Nat. Energy* *5*, 478–486.
- 404 18. Yang, P.-P., Zhang, X.-L., Gao, F.-Y., Zheng, Y.-R., Niu, Z.-Z., Yu, X., Liu, R., Wu, Z.-Z.,  
405 Qin, S., Chi, L.-P., et al. (2020). Protecting Copper Oxidation State via Intermediate  
406 Confinement for Selective CO<sub>2</sub> Electroreduction to C<sub>2+</sub> Fuels. *J. Am. Chem. Soc.* *142*, 6400–  
407 6408.
- 408 19. Ma, W., Xie, S., Liu, T., Fan, Q., Ye, J., Sun, F., Jiang, Z., Zhang, Q., Cheng, J., and Wang,  
409 Y. (2020). Electrocatalytic reduction of CO<sub>2</sub> to ethylene and ethanol through hydrogen-  
410 assisted C–C coupling over fluorine-modified copper. *Nat. Catal.* *3*, 478–487.
- 411 20. Perry, S.C., Gateman, S.M., Malpass-Evans, R., McKeown, N., Wegener, M., Nazarovs, P.,  
412 Mauzeroll, J., Wang, L., and Ponce de León, C. (2020). Polymers with intrinsic microporosity  
413 (PIMs) for targeted CO<sub>2</sub> reduction to ethylene. *Chemosphere* *248*, 125993.
- 414 21. Ma, M., Clark, E.L., Therkildsen, K.T., Dalsgaard, S., Chorkendorff, I., and Seger, B. (2020).  
415 Insights into the carbon balance for CO<sub>2</sub> electroreduction on Cu using gas diffusion electrode  
416 reactor designs. *Energy Environ. Sci.* *13*, 977–985.
- 417 22. Li, F., Thevenon, A., Rosas-Hernández, A., Wang, Z., Li, Y., Gabardo, C.M., Ozden, A.,  
418 Dinh, C.T., Li, J., Wang, Y., et al. (2020). Molecular tuning of CO<sub>2</sub>-to-ethylene conversion.  
419 *Nature* *577*, 509–513.
- 420 23. Gabardo, C.M., O’Brien, C.P., Edwards, J.P., McCallum, C., Xu, Y., Dinh, C.-T., Li, J.,  
421 Sargent, E.H., and Sinton, D. (2019). Continuous carbon dioxide electroreduction to  
422 concentrated multi-carbon products using a membrane electrode assembly. *Joule* *3*, 2777–  
423 2791.

